MESH REQUIREMENT INVESTIGATION FOR 2D AND 3D AERODYNAMIC SIMULATION OF VERTICAL AXIS WIND TURBINES

SAMAN NAGHIB ZADEH

A Thesis

In the Department

of

Mechanical and Industrial Engineering

Presented in Partial Fulfillment of the Requirements
for the Degree of
Master of Applied Science (Mechanical Engineering) at
Concordia University
Montreal, Quebec, Canada

June 2013

Concordia University

School of

Graduate Studies

This is to certify that the thesis prepared

By: **Saman Naghib Zadeh**

Entitled: Mesh Requirement Investigation for 2D and 3D Aerodynamic Simulation of Vertical Axis Wind Turbines

and submitted in partial fulfillment of the requirements for the degree of

Master of Applied Science (Mechanical Engineering)

Complies with regulation of the university and meets the acceptable standards with respect to originality and quality.

Signed by the final examining committee:

Mehdi Hojjati Chair

Ali Dolatabadi Examiner

Luiz A.C. Lopes Examiner

Marius Paraschivoiu Supervisor

Approved by

MASc Program Director

Department of Mechanical and Industrial Engineering

2013

Dean of Faculty

Abstract

Mesh Requirement Investigation for 2D and 3D Aerodynamic Simulation of Vertical Axis Wind Turbines

Saman Naghib Zadeh

The accuracy of a Computational Fluid Dynamics (CFD) model to capture the complex flow around a small vertical axis wind turbine (VAWT) on 2D and 3D grids is investigated. The aerodynamic complexity of the flow is mostly due to rapid variation of the angle of attack of the rotating blades. The resulting flow includes large separation flows over the blades, dynamic stall, and wake-blade interaction. These features are sensitive to the grid resolution and turbulence models. In the present research, a grid convergence study is conducted on 2D grids to examine the CFD model sensitivity to mesh resolution and to identify when grid convergence is obtained. An averaged-grid size of $y^+ > 30$ is employed along the wall to capture the near-wall region flow structures. Moreover, a parallel OpenFOAM solver is used to investigate the numerical solution of Unsteady Reynolds-Averaged Navier-Stokes (URANS) equations coupled with Spalart-Allmaras (SA) turbulence model. As a result, it is seen that the Power Coefficient (C_p), in 2D investigations, increases with the mesh size until it achieves grid convergence. For a 3D simulation, only a coarse mesh can be used due to large computational requirements. It is found that the 3D coarse mesh significantly under-predicts the Power Coefficient but is able to predict tip vortices.

ACKNOWLEDGEMENTS

This research would have not been possible without the support and supervision of Dr. Paraschivoiu. His encouragements towards this work are greatly acknowledged.

This work is dedicated to my devoted mother and,
the eternal soul of my father.

Table of Contents

List of Figures

List of Tables

Nomenclature

α	Angle of Attack
ψ	Azimuthal angle
λ	Tip Speed Ratio
ω	Angular velocity of the rotor
f_v	Closure function
$\tilde{v}$	Modified kinematic eddy viscosity
v	Kinematic molecular viscosity
ρ	Density of fluid
Ω	Magnitude of vorticity
C_v	SA constant
$\tilde{s}$	SA production term
κ	Kappa
SO_2	Sulfur Dioxide
NO_2	Nitrogen Dioxide
CO_2	Carbon Dioxide
ε	Turbulence Dissipation Rate
k	Turbulence Kinetic Energy
C	Chord Length
C_p	Power coefficient
Re	Reynolds Number
CFD	Computational Fluid Dynamics

1. Introduction

In this chapter

An introduction to various types of wind turbines is presented. In addition, the benefits of employing Vertical Axis Wind Turbines and modeling this phenomenon with CFD will be discussed in details, and finally the objectives and thesis organization will be explained.

1.1. Wind Turbines

Wind turbines are classified based on their axis of rotation. Basically, there are two types of wind turbines, namely Horizontal Axis Wind Turbines (HAWTs) and Vertical Axis Wind Turbines (VAWTs). The majority of currently installed wind turbines belongs to HAWTs. However, some important advantages of VAWTs make them to be widely applicable in urban areas. A VAWT is a type of wind turbine which has the main rotor located vertically and the gear box is placed near the ground. Therefore, in comparison with HAWTs, maintenance and repair level compliance requirements are facilitated. In addition to the maintenance facility, VAWTs provide significant advantages which make them to be a better choice. Most importantly, VAWTs can be placed close to each other. As a result, less space is occupied compared to HAWTs. Furthermore, less noise is produced and also the starting speed to move the blades is much less than HAWTs. Generally, HAWTs provide better performance in the uniform wind but their performance becomes less as the wind direction fluctuates [1]. Hence, for any direction, non-uniformity or even the rapid fluctuations of the wind, VAWTs operate better [2] and also, dirty winds have less effects on their performance. Besides, VAWT blades have a uniform and untwisted profile which makes their fabrication easier compared to HAWTs which blade should be tapered and twisted in order to gain the optimal efficiency. The major drawbacks are the lack of self-starting capability as well as its high torque fluctuations within each revolution cycle [3] [4]. Moreover, due to rotational motion of the wind turbines, dynamics stall and fatigue failure may occur.

1.2. Motivation

Wind turbines have become the symbol of clean energy over the last years. In fact, unlike most other technologies for generating electricity, wind turbines do not utilize combustion processes which yields environmentally hazardous emissions. Basically, employing fossil fuels in power plants, to generate electricity, causes a considerable increase of the greenhouse effect. This is because, the Carbon Dioxide (CO_2) is released to the atmosphere. According to the experimental published data [2], in order to generate 1 kWh of electricity, 1 kg of CO_2 is released. Another important parameter from an environmental point of view is considered to be acid rains, which is caused by the existence of the Sulfur Dioxide (SO_2) and Nitrogen Dioxide (NO_2) in the air. Therefore, in order to cope with these environmental problems, Renewable and Nuclear energies are suggested and utilized as desirable alternatives. It should be stated that the renewable energy is referred to the type of energy which is obtained from the natural resources and can be used repeatedly. Generally, there are various types of renewable energies which are used to generate electricity, namely solar, wind energy, hydroelectricity etc. Wind energy is one of the major resources of electricity generation, among all the other renewable energies and after hydro power [5]. In fact, the general idea is to convert the wind energy to the mechanical form of the energy. It should be mentioned that, wind turbines provided 1.5 % of the worldwide electricity usage in 2008. As it can be clearly predicted, the promising development of the wind energy is expected in the next two decades [6]. As a result, it has been acknowledged that the wind global cumulative wind power capacity will be increased up to 832,251 MW and 1,777,550 MW in the years 2020 and 2030, respectively. It should be taken into account that the computed capacity in 2009 was approximately 158,505 MW. By means of this quantitative comparison, it can be concluded that the wind power provides approximately 6th of the world electricity. This comparison has been made on land and offshore wind farms as well as the industrial wind turbines.

In order to fulfill the needs of wind industry, research and investigation, in aerodynamics and structural analysis, suitable installation location etc., should be carried out. Regarding the aerodynamics analysis, the blade type and profile of wind turbines play key roles for achieving a desirable power, analyzing and determining a proper angle of attack. In order to gain the maximum efficiency it is required to study the aerodynamics characteristics of a blade which consequently yields an accurate distribution of aerodynamics forces around the blade.

The equations which are governing the complex flow around wind turbines are the Navier-Stokes equations. In order to analyze the behavior of the flow around a wind turbine experimental or numerical techniques are employed. However, performing experimental analysis require incompressible wind tunnels as well as appropriate and reliable equipment for the phase of data acquisition. Therefore, because of the expenses of wind tunnels and their tools, it is necessary to look for an alternative solution which provides relatively fast, accurate and reliable results.

Nowadays, engineers and researchers perform the flow analysis based on Computational Fluid Dynamics (CFD). This is because, the complex flow around a VAWT can be investigated in more details by employing CFD models. Therefore, numerical analysis is considered to be a desirable alternative to capture the complex flow phenomena over a

VAWT. In order to simulate the flow, CFD employs a set of numerical techniques to solve the Partial Differential Equations (PDEs). For this purpose, a variety of models such as Reynolds Averaged Navier-Stokes (RANS) or Large Eddy Simulations (LES) models can be utilized. Although, in CFD analysis the ability to capture all the relevant physics and flow features, e.g., separation of boundary layer, may be difficult to achieve, it still predicts aerodynamics parameters, e.g., the coefficient of power.

1.3. Aims and Objectives

Output power of VAWTs can be achieved based on two different concepts. The first concept expresses the generation of electricity using the drag force over the blades which is known as the Savonius VAWT, whereas, in the second approach, lift is the main acting force to turn the blades along the axis of rotation which is known as the Darrieus/Giromill VAWT. Figure 1.1 shows various types of wind turbines.

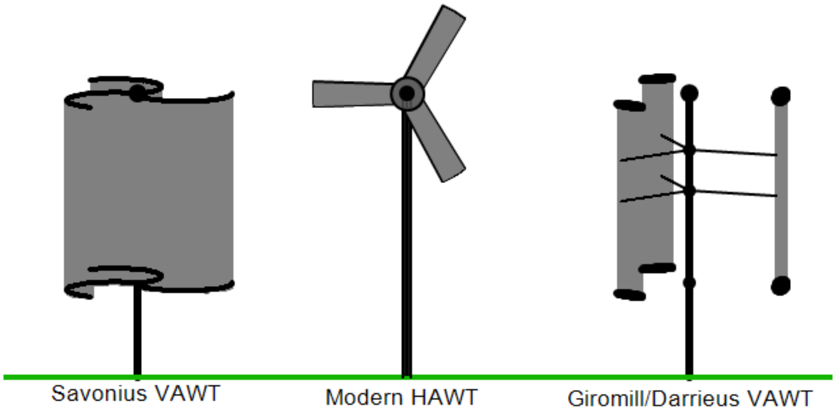

Figure 1.1. Three primary types of wind turbines [7]

In this thesis, WHI model 530G VAWT, Figure 1.2, is considered for the numerical analysis. The wind turbine is rated at 25 kW at wind speeds of 8 m/s.

Figure 1.2. WHI model 530G VAWT [8]

Hence, the simulation of flow over Giromill wind turbine is investigated in this numerical computation. The major objective of this study is to determine the mesh sensitivity for both 2D and 3D CFD analysis of flow over the VAWT blades. In fact, due to the complex aerodynamics and huge amount of variations in turbulent length scale, it has become one the most important issues in today's numerical investigations. The parameters and phenomenon that make CFD prediction much more challenging can be categorized as; separation of flow, highly turbulent flow on the blades, dynamic stall, vortex shedding of the tips of the blades and the unsteady downstream wakes. These features are sensitive to the mesh and turbulence models. In this work, only the mesh size is investigated. In order to fulfill this objective, CFD analysis has been performed based on Unsteady Reynolds Averaged Navier-Stokes (URANS) equations coupled with the Spalart Allmaras (SA) turbulence model.

The analysis performed herein is based on a general purpose open source software package, OpenFOAM, to capture the complex flow over VAWTs. Martin Beaudoin from the Hydro Quebec Research Institute in Montreal and Hrvoje Jasak from Wikki Ltd have been developing a Semi-Implicit Pressure Linked Equation (SIMPLE) based transient solver for turbo-machinery and wind turbine analysis as well as a coupling interface which was previously introduced by Hrvoje Jasak in the early version of OpenFOAM known as General Grid Interface (GGI) scheme. This method can be implied to couple multiple non-conformal regions into a single continuous domain and can be used as a common interface in Turbo-machinery simulations [9].

OpenFOAM was set up to estimate the efficiency of the VAWT by calculating the Coefficient of Power (C_p). Basically, the output power of a wind turbine demonstrates how efficiently the wind energy is converted into electricity. It should be stated that C_p is computed by means of the total tangential forces of the blades after certain number revolutions.

The investigation and exploration of the vorticity structures is presented in this work. Since, the blades are rotating in each time step, a discussion of the dynamic stall, vortex shedding as well as tip vorticity structure in 3D is appropriate. The main contribution is the spatial convergence analysis that is carried out to investigate the independency of results to mesh resolution in the verification phase as well as comparison between 2D and 3D.

1.4. Thesis Organization

Chapter 2: Aerodynamics background of wind turbine is covered. In addition, the structures of vorticity, dynamic stall and turbulence modeling of VAWTs are presented and finally, CFD simulation of wind turbines is considered.

Chapter 3: An overview on the governing equations associated with VAWTs is presented. In addition, the computational model to analyze the turbulence structures is studied. Finally, the advantages of modeling this phenomenon in OpenFOAM will be explained.

Chapter 4: A grid convergence investigation is performed to ensure the independency of the solution to the grid resolution in the verification phase. Afterwards, in the validation phase the results of the numerical analysis are quantitatively validated with the experimental techniques.

Chapter 5: The velocity and vorticity structures as well as the variation of torque against azimuthal angle, for the 2D mesh, at different TSRs, are presented.

Chapter 6: The 3D flow structure is presented and the obtained 2D and 3D results are compared.

Chapter 7: The closure part of this numerical study, achieved goals, overall conclusion of this work and also the future works are discussed.

2. Aerodynamics Background

In this chapter

The aerodynamics background of wind turbine is covered. In addition, the structures of vorticity, dynamic stall and turbulence modeling of VAWTs are presented and finally, CFD simulation of wind turbines is considered.

2.1. Vorticity Structures and Dynamic Stall

One of the most essential issues in 3D computation of VAWTs is the existence of various types of vortices in the domain. Basically, the important influence of the vortices can be characterized as the distribution of bound vortex in span-wise direction, decreased convection velocity of the wake due to induced trailing vorticity and the tip vortex development as a function of azimuthal angle [10]. Furthermore, trailing vortices has played an important role in the determination of the strength of the VAWTs. This is because, the investigation of the formation of tip vortex and its downstream distribution could greatly improve the placement of multiple VAWT. In fact, the complex flow feature is observed due to the interaction of the separation of the flow and tip vorticity under the static and dynamic stall conditions. Therefore, the efficiency of the VAWT can be dramatically influenced by the complex flow structure.

Despite the advantages of VAWTs in various aspects, the aerodynamics characteristics are complex in the near blade area compared to HAWTs. One important challenge in developing a mathematical model for a VAWT simulation is the dynamic stall phenomenon which usually occurs at low TSRs. In fact, due to its direct effect on the output torque, generated by turbine blades, it has become one of the most important parameters in VAWTs computation. When an airfoil is moving, e.g., a wind turbine blade, due to the rapid and consecutive change of angle of attack, the static stall values are no longer valid. Moreover, power generation at low TSRs can be greatly enhanced, however, due to vortex generation, some other problems such as noise and vibrations may arise [11]. The numerical investigation of flow passed a VAWT was analyzed by Simao Ferreira et al. [12] [13] to study the dynamic stall by employing various types of turbulence models. It was observed that by considering fully turbulent assumption the maximum normal force on the blades is considerably decreased. Moreover, it was seen that the employed turbulence models were not able to correctly capture the large eddies within the domain. It was also declared that validation phase was not fulfilled due to the lack of experimental data of the VAWT.

Basically, dynamic stall occurs due to the pitch motion of an airfoil in a free stream velocity which yields the formation of an organized vortex shedding pattern. Dynamics stall can be characterized and formed by the following sequential stages [10]:

Stage1: A reversal flow pattern is developed at the trailing edge and moved towards the leading edge after the static stall angle.

Stage 2: The separation point is moved forward to the leading edge due to the increase of incidence angle. The separation of boundary layer causes the drag to increase. Besides, the center of pressure is travelled downstream causing the pitch down condition for the blade. Consequently, a dynamic stall vortex is generated due to the layer which was formed at the leading edge and rolled up.

Stage 3: The maximum value of lift is reached and the dynamic stall vortex is grown due to the accumulation of vortices which were generated at the leading edge separation.

Stage 4: Lift value is dropped and separation is taken place as a result of the dynamic stall vortex which left the surface of the blade. As the pitch rate is increased, the growth of vortex shedding at the leading edge is greatly observed.

Stage 5: As the incidence angle is decreased, the reattachment phase is taken place and the flow is reattached from the leading edge towards the trailing edge.

2.2. Turbulence Modeling

The CFD Investigation of oscillating airfoils by utilizing different types of turbulence models has been conducted by Wang et al. [14] [15] to capture the dynamic stall. It was seen that $k-\omega\ SST$ turbulence model with Detached Eddy Simulation (DES) approach is more accurate to predict the dynamic stall compared to $k-\omega\ Standard$, $k-\omega\ SST$ and $RNG\ k-\varepsilon$ models. Moreover, Simao Ferreira et al. [16] have conducted a numerical analysis by comparing the results among the URANS, LES and DES turbulence models. It was clearly seen that turbulence models have a great influence on the prediction of the dynamic stall on the VAWT.

Moreover, Digraskar [17] has conducted a numerical simulation of wind turbines by employing the SA turbulence model implemented in OpenFOAM. The obtained results clearly demonstrated a desirable prediction of aerodynamics parameters of the wind turbine. However, regarding the dynamic stall, the separation over the blade surface was not captured.

In this thesis, the SA model, because of its simplicity, is used as a turbulence model to perform the numerical analysis. Basically, Spalart and Allmaras [18] introduced a new turbulence modeling method in 1992. The major reason for developing this model was the applications in aerodynamics fields such as turbo-machinery and aerospace systems. In fact, one of the most important advantages of using this method is the ability to compute the boundary layer flow in the presence of adverse pressure gradients. Generally, surface curvature is the main reason of having the adverse pressure phenomenon. One of the most common curved profile shapes which has a variety of applications in aerospace industry, e.g., typical shape of the airplane fuselage as well as turbine blades, is airfoil. Nowadays, SA is known as one of the desirable models in wind turbine studies. This is because, compared to all the other turbulence models, implied in this area, such as $k-\omega\ SST$ model and LES, it is not expensive and results are in a good agreement with the experimental data [19]. More explanations regarding SA model is presented in the governing equation section.

2.3. CFD Simulation of Wind Turbines

The aerodynamic characteristics of a small HAWT were analyzed by Tachos et al. [20]. RANS equations coupled with SA turbulence model was used as governing equations in FLUENT software. The preliminary flow feature regarding the wake generation at the downstream of turbine was visualized. Since, the flow was fully turbulent, the considered model failed to compute the experimental power curves. The commercial code, FLUENT, was used to simulate an air flow over a prototype micro HAWT by Menteiro et al. [21]. The purpose of this study was to investigate the numerical solution of RANS equations combined with $k-\varepsilon$ turbulence model followed by standard wall function. Moreover, power and efficiency of the rotor as well as the pressure variation around three sections of the span of the blade were analyzed. However, in the phase of validation, lack of comparing numerical results against the experimental techniques was one of the most important issues in the results.

On the other hand, 2D and 3D numerical computations have been carried out by Hamada et al. [22] in 2008 regarding an H–VAWT by means of FLUENT software. The verification analysis, including the mesh independency and time step investigation, was performed on a mesh utilizing different types of $k - \varepsilon$ turbulence models, however, the results were not experimentally validated. Furthermore, 3D results demonstrated a significant decrease in power coefficient. This is because, in the 3D model, the central shaft and arm wakes, tip vortices as well as the mesh density were taken into consideration. Consequently, it was clearly seen that the major drawback was the lack of experimental data for the validation.

Edwards et al. [23] and Howell et al. [24] have performed the similar investigations and observed the same behavior in terms of 2D and 3D performance analyses. The Reynolds Number employed by Howell et al. [24] was about 30,000 and only half of the domain with respect to the horizontal axis was simulated for the VAWT. RNG $k - \varepsilon$ turbulence model followed by wall functions was selected to capture the turbulence features. 3D results showed a good agreement with the experimental results while the C_p values were considerably high in 2D analysis. Similarly, validation was not performed for the numerical model.

Moreover, CFX solver was employed by Mclaren et al. [25] to analyze the dynamic tangential and radial forces of the blades of a wind turbine. In order to calculate the Aerodynamics parameters such as lift and drag forces on the blades, $k - \omega\ SST$ model coupled with $\gamma - \theta$ was used. The obtained numerical results were compared to a set of quasi steady state data and it was seen that the transitional model was able to capture the important features of the flow.

In terms of validation, a set of experimental tests were carried out by Edwards et al [26]. It was observed that $k - \omega\ SST$ turbulence model perfectly determines the flow structure in unsteady simulation of pitching airfoils. Particle Image Velocimetry (PIV) visualizations were used as a tool for validation at three different TSRs. Based on the obtained results, the increase of C_p values for the 2D analysis was similarly observed compared to experimental data.

On the other hand, three different approaches, namely, Blade Element Momentum (BEM), RANS and Vortex Lattice (VL), were employed to investigate the Aerodynamics characteristics of flow over a HAWT by Duque et al. [27] [28]. The obtained results illustrated a good agreement with the experimental data at pre-stall condition. Since, Baldwin-Barth method was used to capture the turbulence structures in RANS equations and fully turbulent assumption was made, simulation failed to provide the correct result near blade stall.

Hence, in order to perform the numerical investigation of flow over VAWTs, it is required to perform a rigorous mesh study and also, understand 2D and 3D differences.

3. Methodology

In this chapter

An overview on the governing equations associated with VAWTs is presented. In addition, the computational model to analyze the turbulence structures is studied. Finally, the advantages of modeling this phenomenon in OpenFOAM will be explained.

3.1. Governing Equations

In this thesis the simulation of flow over the VAWT is studied by seeking the numerical solution of URANS equations coupled with SA turbulence model. The incompressible Navier-Stokes equations for Newtonian fluids are,

$$\frac{\partial u_i}{\partial x_i} = 0 \tag{3 − 1}$$

$$\frac{\partial u_i}{\partial t} + \frac{\partial}{\partial x_j}\left(u_i u_j\right) = -\frac{1}{\rho}\frac{\partial P}{\partial x_i} + \vartheta\frac{\partial^2 u_i}{\partial x_j} \tag{3 − 2}$$

In order to derive URANS equations, Reynolds decomposition is carried out. Hence, the instantaneous flow variable, e.g., velocity component u_i, is expressed as the sum of the mean, $\overline{u_i}$, and the fluctuating components, $u_i{}'$, i.e.

$$u_i = \overline{u_i} + u_i{}' \tag{3 − 3}$$

Similarly, pressure is also decomposed into the time-averaged value, $\overline{p}$, and the fluctuating pressure, p'.

Applying Reynolds decomposition and taking time-average of the continuity and momentum equations yields the following URANS equations as follows,

$$\frac{\partial \overline{u}_i}{\partial x_i} = 0 \tag{3 − 4}$$

$$\frac{\partial \overline{u}_i}{\partial t} + \frac{\partial}{\partial x_j}\left(\overline{u}_i \overline{u}_j\right) = -\frac{1}{\rho}\frac{\partial \overline{P}}{\partial x_i} + \upsilon\frac{\partial^2 \overline{u}_i}{\partial x_j} + \frac{\partial \tau_{ij}}{\partial x_j} \tag{3 − 5}$$

Where, $\overline{P}$ and $\overline{u}_i$ are the averaged pressure and velocity components, respectively. υ is the kinematic viscosity and ρ is the density of fluid. Furthermore, τ_{ij} is the specific Reynolds Stress tensor and can be described as,

$$\tau_{ij} = -\overline{u'_i u'_j} \qquad (3-6)$$

This is an additional symmetric tensor which has six independent components and expresses the correlation between the fluctuating velocities. Basically, for 3D flows, there are four equations and ten unknowns including six components for Reynolds stress, one pressure and three velocities. Therefore, in order to close the system, more equations are needed.

3.2. Turbulence Modeling

The next approach is to employ SA turbulence model as an additional transport equation. In this model the kinematic eddy viscosity term is expressed by the following equation:

$$\upsilon_t = \tilde{\upsilon} f_{\upsilon 1} \qquad (3-7)$$

Where, $\tilde{\upsilon}$ and $f_{\upsilon 1}$ are the modified kinematic eddy viscosity and closure function, respectively, and can be expressed by,

$$f_{\upsilon 1} = \frac{\chi^3}{\chi^3 + {C_{\upsilon 1}}^3} \qquad (3-8)$$

$$\chi = \frac{\tilde{\upsilon}}{\upsilon} \qquad (3-9)$$

Here, υ is the kinematic molecular viscosity and $C_{\upsilon 1}$ is a constant. The transport eddy viscosity equation in SA model can be defined by the following formula:

$$\frac{\partial \tilde{v}}{\partial t} + U_j \frac{\partial \tilde{v}}{\partial x_j} = C_{b1}\tilde{s}\tilde{v} - C_{w1} f_w \left(\frac{\tilde{v}}{d}\right)^2 + \frac{1}{\sigma}\frac{\partial}{\partial x_k}\left[(v+\tilde{v})\frac{\partial \tilde{v}}{\partial x_k}\right] + \frac{C_{b2}}{\sigma}\frac{\partial \tilde{v}}{\partial x_k}\frac{\partial \tilde{v}}{\partial x_k} \qquad (3-10)$$

In this equation, the first three terms on the right hand side are the production, destruction and diffusion of kinematic eddy viscosity, respectively. The diffusion term includes both the molecular viscosity and the turbulent structures effect.

$\tilde{s}$ represents the production term which is,

$$\tilde{S} = f_{v3}\Omega + \frac{\tilde{v}}{k^2 d^2} f_{v2} \qquad (3-11)$$

Where, Ω corresponds to the magnitude of vorticity and d is the point field distance to the nearest wall, and

$$f_{v2} = \frac{1}{(1+\chi/c_{v2})^3} \qquad (3-12)$$

$$f_{v3} = \frac{(1+\chi f_{v1})(1-f_{v2})}{\chi} \qquad (3-13)$$

The destruction function can be defined as,

$$f_w = g\left(\frac{1+{C_{w3}}^6}{g^6+{C_{w3}}^6}\right)^{1/6} \qquad (3-14)$$

Where,

$$g = r + C_{w2}(r^6 - r) \qquad (3-15)$$

$$r = min\left[\frac{\tilde{v}}{\tilde{S}k^2 d^2}, 10\right] \qquad (3-16)$$

The constants correspond to SA model are listed in Table 3.1.

Table 3.1. SA model coefficient

$C_{b1} = 0.1355$	$C_{v1} = 7.1$
$C_{b2} = 0.622$	$C_{v2} = 5.0$
$C_{w2} = 0.3$	$k = 0.41$
$C_{w3} = 2.0$	$\sigma = 2/3$

3.3. Non-Dimensional Parameters

In this section, it is intended to define the key parameters in wind turbine analysis which are employed in this numerical investigation.

3.3.1. Tip Speed Ratio (TSR)

One important parameter in wind turbine investigations is Tip Speed Ratio (TSR), which is defined as the ratio of tip speed of the blade to the wind speed,

$$\lambda = \frac{R\omega}{V} \qquad (3-17)$$

Where, λ is the TSR, R is the radius of rotor, ω is the angular velocity of turbine, and V is the wind velocity.

3.3.2. Power Coefficient (C_p)

Power coefficient (C_p) is considered to be another important parameter, which can be derived by applying Pi-Buckingham theorem, and is given by,

$$Cp = \frac{P}{\frac{1}{2}\rho A V^3} \qquad (3-18)$$

Here, P is the Power, ρ is the wind density, A is the swept area, and V is the free stream velocity. In order to calculate C_p for various TSRs, a fixed angular velocity of 90 rpm but different wind velocities are employed. The torque is calculated by means of the developed code in OpenFOAM, defined as the sum of the forces acting on each blade. In order to compute the coefficient of power a one meter span is assumed for the swept area calculation.

3.3.3. Azimuthal Angle

The final position of an airfoil with respect to its initial position is defined as Azimuthal angle, Figure 3.1. The corresponding equation which relates angle of the attack of the blade, TSR and azimuthal angle [30] is expressed as,

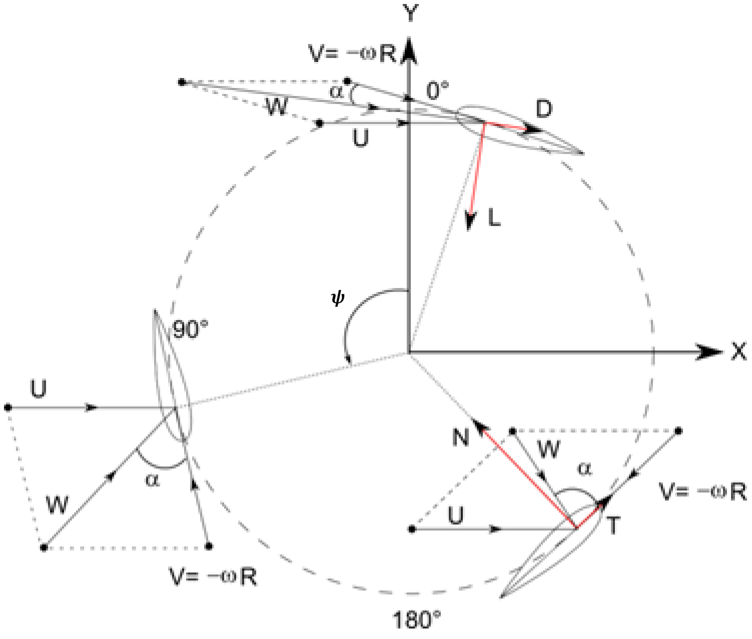

Figure 3.1. Azimuthal angle illustration [30]

$$\alpha = arctan\left(\frac{sin\psi}{\lambda - cos\psi}\right) \qquad (3-17)$$

Where, α is the angle of attack and ψ is the azimuthal angle.

3.4. Numerical Setup

This section considers the numerical setup including the computational model, mesh generation, boundary conditions and case settings employed for both 2D and 3D simulations.

3.4.1. Computational Model

There are two major steps in achieving the numerical solutions namely, pre-processing and post-processing. Basically, pre-processing step consists of building geometry as well as generating mesh which will consequently be converted to a readable format for the solver. As far as, the computational cost is concerned, this part is the most time consuming part in CFD analysis.

3.4.2. Mesh Generation

As it was previously stated, the major step in CFD analysis is to develop an accurate mesh for the computational domain. In fact, in the majority of solvers, the accuracy of the numerical results strongly depends on the quality of the employed mesh. Basically, there are two types of meshes in CFD investigations, namely, structured and unstructured grids. Structured types of grids are sets of elements which are repeated in a regular pattern with respect to space and are demonstrated by quadrilateral elements in 2D and hexahedral elements in 3D. Due to this regular arrangement, each cell can be directly addressed by means of an index (i, j) and (i, j, k) in 2D and 3D, respectively, which yield to save lots of computational efforts during the computation [17].

Grids of this type are widely applicable in CFD analysis especially in finite difference method. This is because, the variables differentiations can be expressed conveniently as finite difference approach is employed. On the other hand, arbitrary shaped elements can be utilized in unstructured mesh. Grids of this type are mostly implied for finite element and volume computation. This is because of their ability to resolve finely around complex physical geometries. These types of grids are mainly represented by triangles and tetrahedrons in 2D and 3D, respectively. Due to irregular repeating pattern, the connectivity information is stored explicitly. Since, an extra memory is required for storing the connectivity information of the mesh, additional computational cost is expected.

In the present work, unsteady flow simulations are performed for 2D and 3D computational domains of the VAWT with the geometry specifications given inTable 3.2. It should be mentioned that the 3D effects such as struts and tip blade effects are neglected in 2D analysis. Gambit software is used as a tool for creating the geometry and mesh generation.

Table 3.2. Specification of the geometry

Number of rotors	1
Number of blades	4
Blade chord	0.4445 m
Rotor Diameter (D)	5.395 m
Angular velocity of the rotor	90 rpm
The diameter of the rotating zone	1.053 D

The computational domain of a VAWT includes two main zones, namely, stationary zone, which is considered for the far field flow and the rotating zone, that rotates with four NACA 0018 blades with the given angular velocity. A rectangular domain, which corresponds to the stationary zone, is utilized, for 2D grid, with a distance of 10 rotor diameter from the axis of rotation to top, bottom and left boundaries (Figure 3.2). Also there is 15 rotor diameter distance from the axis of rotation to outflow boundary. Figure 3.2 and Figure 3.3 illustrate the mesh of the computational domain as well as the mesh around an airfoil, respectively. Bottom-Up approach is used to make the 3D grid. In this technique the vertices, edges, faces are first created in 2D and thereafter 3D meshes and volumes are constructed. The 2D domain is extended by 1.71 chords in span-wise direction, 1/2 of one level, Figure 1.2, and after that the grid is extruded another 1.71 chord from the tip of blade to the front in z-direction, Figure 3.4.

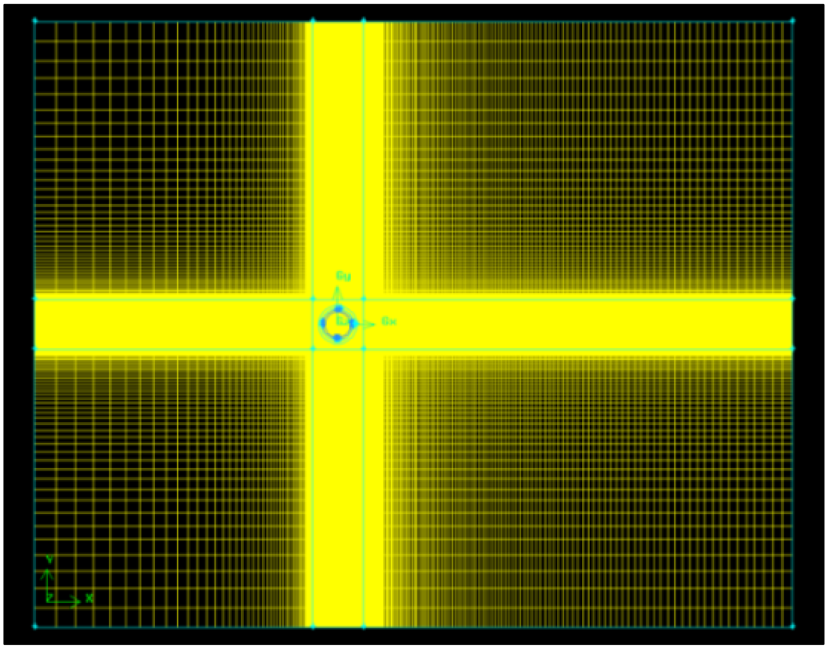

Figure 3.2. Mesh of the computational domain

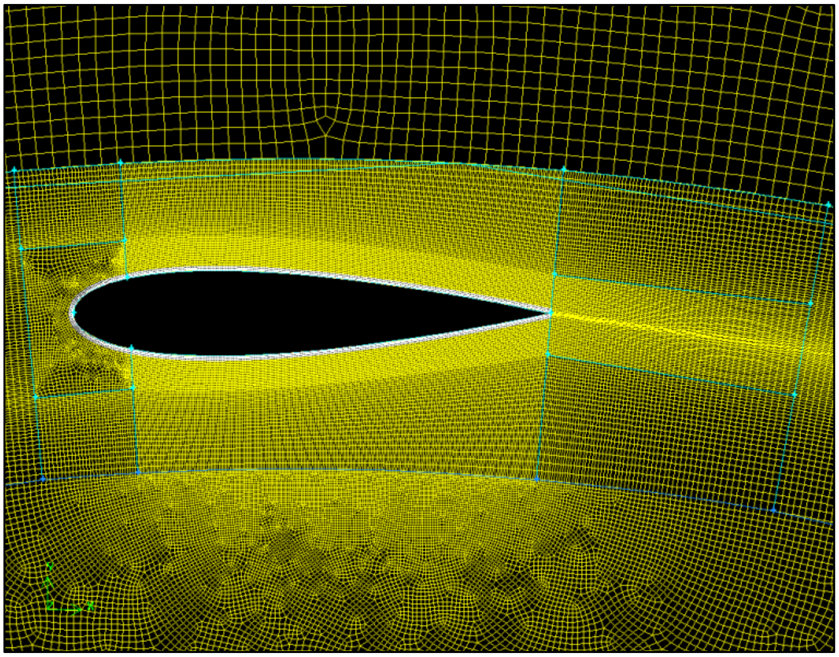

Figure 3.3. A typical generated mesh around an airfoil

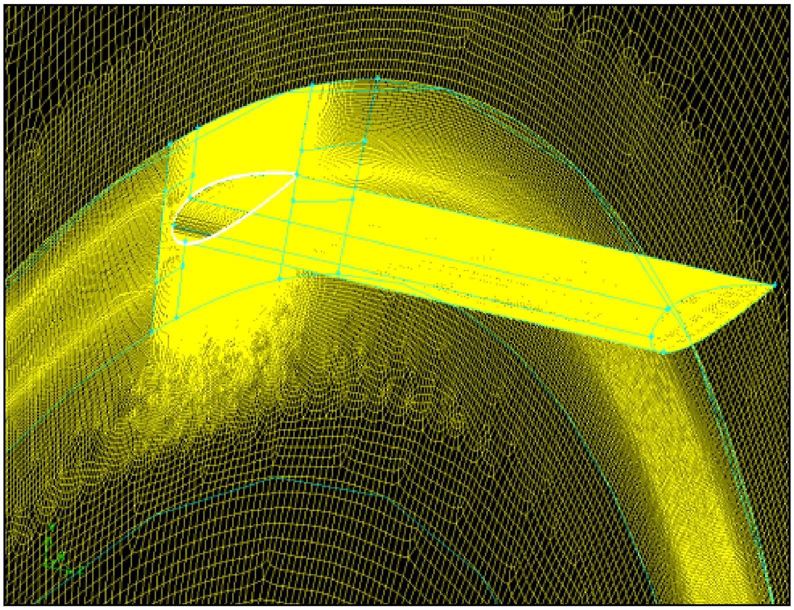

Figure 3.4. 3D mesh representation of the domain

3.4.3. Boundary Conditions

In order to conduct CFD analysis, it is necessary to specify initial and boundary conditions for the domain. According to Figure 3.5, a fixed value is set for velocity at the far-field boundary in upstream of rotor and atmospheric pressure is specified for the pressure at the downstream boundary. Moreover, symmetry boundary condition is applied on the sides and no-slip boundary condition is assumed on the blades. In the 3D case, Figure 3.6, the symmetry boundary is chosen for the sides and also, the face which blades are attached, and slip boundary condition is chosen for the front face. The modified kinematic eddy viscosity ($\tilde{\nu}$) is chosen as $\tilde{\nu} = 5\nu$ at the inlet and $\tilde{\nu} = 0$ at the walls, based on the reference [30]. Similarly, turbulent viscosity (ν_t) is computed from Equation (3-7) and set to be $\nu_t = 2.029e-05$ at the inlet.

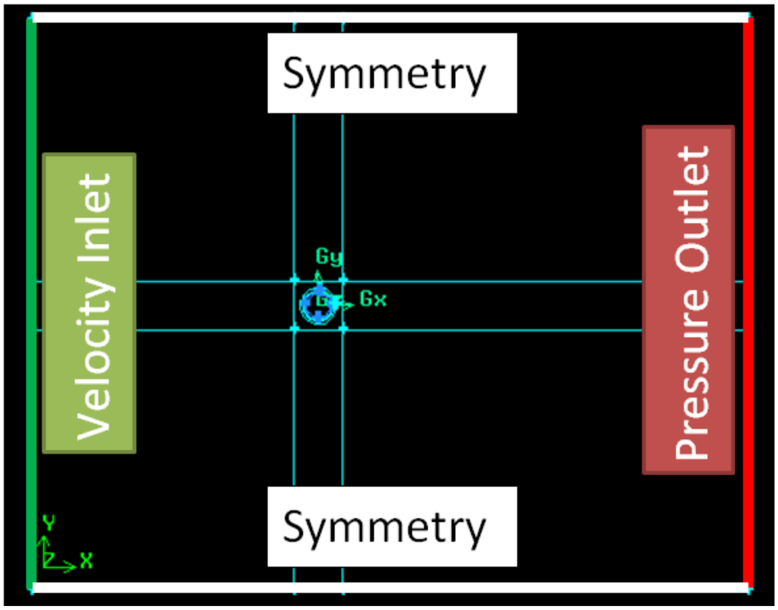

Figure 3.5. 2D boundary conditions

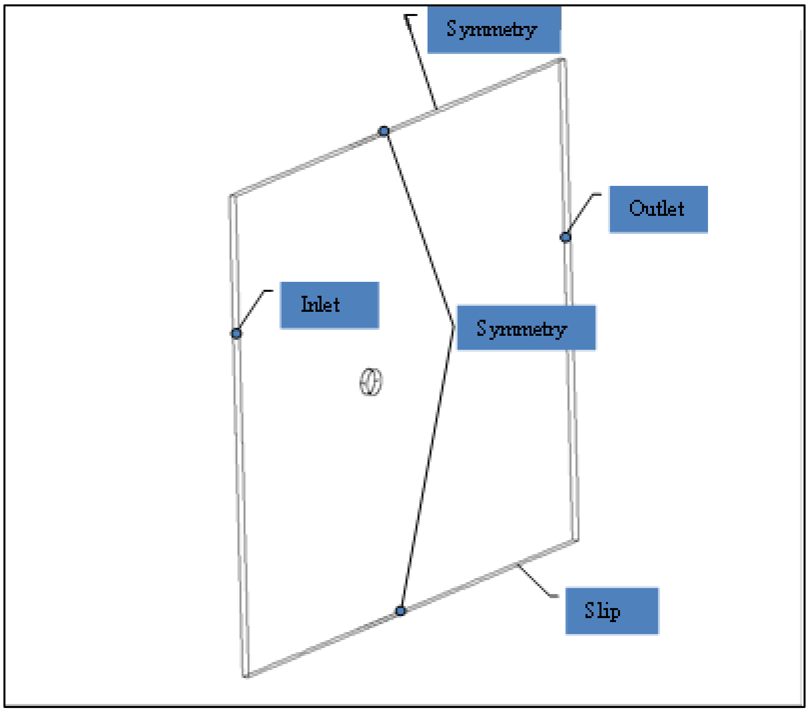

Figure 3.6. 3D boundary conditions

3.4.4. Physical Properties

The working fluid in this analysis is air with the specifications given in Table 3.3.

Table 3.3. Far-field air flow properties

Properties	Value
Kinematic viscosity (ν)	1.57×10^{-5} (m^2/s)
Density (ρ)	1.1774 (kg/m^3)

3.5. OpenFOAM

OpenFOAM, Open Field Operations and Manipulations, is an open source software package including CFD utilities and solvers. In order to deal with CFD problems associated with wind turbines two approaches are employed in OpenFOAM. Basically, in Multi Reference Frame (MRF) approach [17], instead of moving the blades through the mesh, part of geometry is moving relative to the rest of the mesh. One of the most important advantages of using this approach is its fastness compared to other types of methods which involve the mesh motion. This is because, the computation is not performed at each time step for different positions of a mesh since the mesh is always fixed. Hence, this method can be employed in the rotor simulation in which only the non-inertial reference frames exists, e.g., HAWTs. Since the Geometry of VAWTs contains both the rotating and the stationary zone, it is necessary to employ a solver which rotates the mesh around the rotor at each time step. Therefore, an incompressible transient state solver with moving mesh capability is needed to handle both the stationary and rotating part simultaneously [29]. More explanation regarding the employed solver can be found in the next sections.

3.5.1. Discretization Schemes in Time and Space

In order to discretize convection terms in the velocity and turbulence equations, Gauss scheme with upwind interpolation is used. Furthermore, Euler implicit scheme is employed for the time discretization. Pressure gradient is discretized by using Gaussian integration followed by the linear interpolation scheme which uses second-order central differencing. Laplacian terms are discretized by Gaussian integration with linear interpolation of the diffusion coefficient (υ) with a surface normal gradient scheme, which is an explicit non-orthogonal correction. It should be mentioned that the surface normal gradient is computed at the face of the cell and is a component which is normal to the face of the values of gradient at the centers of the two cells that is connected by the face [31].

3.5.2. Solver

In order to solve velocity, pressure and turbulence equations Krylov Subspace Solvers (KSS) are employed. A preconditioned bi-conjugate gradient (PBiCG) solver followed by the diagonal-based incomplete lower-upper (DILU) preconditioner for asymmetric matrices is used for velocity and turbulence equations. For the pressure equation, a preconditioned conjugate gradient (PCG) solver with a Diagonal-based Incomplete Cholesky (DIC) preconditioner, which is used for symmetric matrices, is employed [31].

3.5.3. Pressure-Velocity Coupling

SIMPLE algorithm is mostly used for transient-state simulations to couple the velocity and pressure in OpenFOAM [29]. In this study, the SIMPLE algorithm is utilized for both 2D and 3D numerical computations. This is because, this method has the capability of having larger time steps compared to pressure implicit splitting of operators (PISO) algorithm. In fact, due to the limitation on the maximum time step, the PISO solver is computationally considered to be an expensive solver. The SIMPLE algorithm sequentially performs the following steps:

Step1: Boundary conditions are set

Step2: In order to calculate the intermediate velocity field Discretized momentum equation is computed

Step3: Mass fluxes at the cells faces are calculated and employed

Step4: Pressure equation is computed and under-relaxation factor is applied

Step5: The computed mass flux at the cell faces are corrected

Step6: According to the new pressure, velocity field is corrected

Step7: Boundary conditions are updated accordingly

Step8: The procedure should be repeated untill the convergence criteria is met

3.5.4. General Grid Interface (GGI)

In order to join two non-conformal meshes for the CFD analysis of VAWTs, a coupling interface, namely General Grid Interface (GGI) is employed. In fact, the methodology is to utilize weighted interpolation to compute and transmit the flow variables in the interface region [9]. In OpenFOAM, the patches at the interface are set to be GGI. In the present study, for simulating the flow over the VAWT, a mesh containing two zones is employed. The outer region is the stationary zone and the inner mesh is the rotating zone, hence the treatment of the interface between the stationary and rotating zone is the GGI interface known as GGI master and shadow patch. Generally, in sliding interface, the code performs mesh manipulation after each time step, while, in GGI type of boundary condition, the code performs interpolation between the rotating and the stationary patches of the mesh [17].

4. Verification and Validation

In this chapter

A grid convergence investigation is performed to ensure the independency of the solution to the grid resolution in the verification phase. Afterwards, in the validation phase the results of the numerical analysis are quantitatively validated with the experimental data.

4.1. Verification by Grid Convergence Index (GCI) [32]

In order to prepare a consistent manner in reporting the results of grid convergence, Roache, developed an approach, namely, Grid Convergence Index (GCI), which is based on Richardson Extrapolation (RE) and is considered to be the most acceptable and recommended method employed for the discretization error estimation.

4.1.1. Procedure for Estimation of Discretization Error

In this study grid convergence analysis has been performed among three meshes with the specifications given in Table 4.1. The first step is to provide a grid or mesh size (h) as follows,

$$h = \left[\frac{1}{N}\sum_{i=1}^{N}(\Delta A_i)\right]^{1/2} \qquad (4-1)$$

here, ΔA_i is the area of the ith cell and N is the number of elements used in the computation. In this study, C_p is the key variable and has been the objective of the numerical simulations. For this purpose, based on the experience, a grid refinement factor,

$$r = \frac{h_{coarse}}{h_{fine}} \qquad (4-2)$$

should be greater than 1.3 and the grid refinement procedure is carried out systematically. For a case where three meshes are employed, the calculation of the apparent order p of the method is based on $h_1 < h_2 < h_3$ and,

$$r_{21} = \frac{h_2}{h_1} \qquad (4-3)$$

$$r_{32} = \frac{h_3}{h_2} \tag{4-4}$$

where, $r_{21}$and r_{32} are the grid refinement factors for the first-second and second-third meshes, respectively, and p is expressed by the following equation,

$$p = \frac{1}{\ln(r_{21})}\left|ln|\varepsilon_{32}/\varepsilon_{21}| + q(p)\right| \tag{4-5}$$

$$q(p) = ln\left(\frac{r^{p}{}_{21} - s}{r^{p}{}_{32} - s}\right) \tag{4-6}$$

$$s = 1.sgn\left(\frac{\varepsilon_{32}}{\varepsilon_{21}}\right) \tag{4-7}$$

where, $\varepsilon_{32} = \emptyset_3 - \emptyset_2$, $\varepsilon_{21} = \emptyset_2 - \emptyset_1$and $\emptyset_i$ corresponds to the key variable in the ith mesh. It should be mentioned that for $r = constant$, $q(p) = 0$. On the other hand, extrapolated values of the objective variable can be calculated using the following equation:

$$\emptyset^{21}{}_{ext} = \frac{(r^{p}{}_{21}\emptyset_1 - \emptyset_2)}{(r^{p}{}_{21} - 1)} \tag{4-8}$$

In order to estimate GCI for the fine mesh, the approximate and extrapolated relative errors are described as follows,

$$e_a{}^{21} = \left|\frac{\emptyset_1 - \emptyset_2}{\emptyset_1}\right| \tag{4-9}$$

$$e_{ext}{}^{21} = \left|\frac{\emptyset_{ext}{}^{21} - \emptyset_1}{\emptyset_{ext}{}^{21}}\right| \tag{4-10}$$

$$GCI^{21}{}_{fine} = F_s \frac{{e_a}^{21}}{{r_{21}}^p - 1} \qquad (4-11)$$

where, F_s is the safety factor, and $F_s = 1.25$ for comparison among three meshes [6]. The calculation procedure for three chosen meshes is shown in Table 4.1.

Table 4.1. Calculation of discretization Error

Characteristics	**Coefficient of Power (C_p)**	
	TSR=2	**TSR=3**
Fine Mesh Elements (N_1)	2 569 426	2 569 426
Medium Mesh Elements (N_2)	1 429 690	1 429 690
Coarse Mesh Elements (N_3)	798 919	798 919
r_{21}	1.34	1.34
r_{32}	1.34	1.34
$\emptyset_1$	0.3168	0.2809
$\emptyset_2$	0.3067	0.2796
$\emptyset_3$	0.2784	0.2527
p	3.52	5.36
${\emptyset_{ext}}^{21}$	0.3224	0.2866
${e_a}^{21}$	3.1 %	1.9 %
${e_{ext}}^{21}$	1.7 %	0.48 %
$GCI^{21}{}_{fine}$	2.2 %	0.64 %

Generally, the overall accuracy of the numerical solution can be improved by refining the grids. As a result, according to Table 4.1, the numerical uncertainty in the fine grid GCI for C_p for TSR 2 and 3 are reported as 2.2 and 0.64 percent, respectively. Note that the mesh required to get grid convergence is quite expensive as more than 2.5 M elements are needed.

4.2. y^+ Analysis

In order to capture the near-wall regions flow structures, standard wall function for SA model is employed as follows,

$$\upsilon_t = \upsilon\left(\frac{y^+\kappa}{\ln E\ y^+} - 1\right) \qquad (4-12)$$

where, Kappa ($\kappa = 0.4187$) and $E = 9$ is the additive constant utilized in the logarithmic law of the wall. Using wall function allows us to locate the first point adjacent to the wall in logarithmic zone instead of sub-layer. Therefore, as shown in Figure 4.1, the averaged calculated y^+should be around 30 in all simulations.

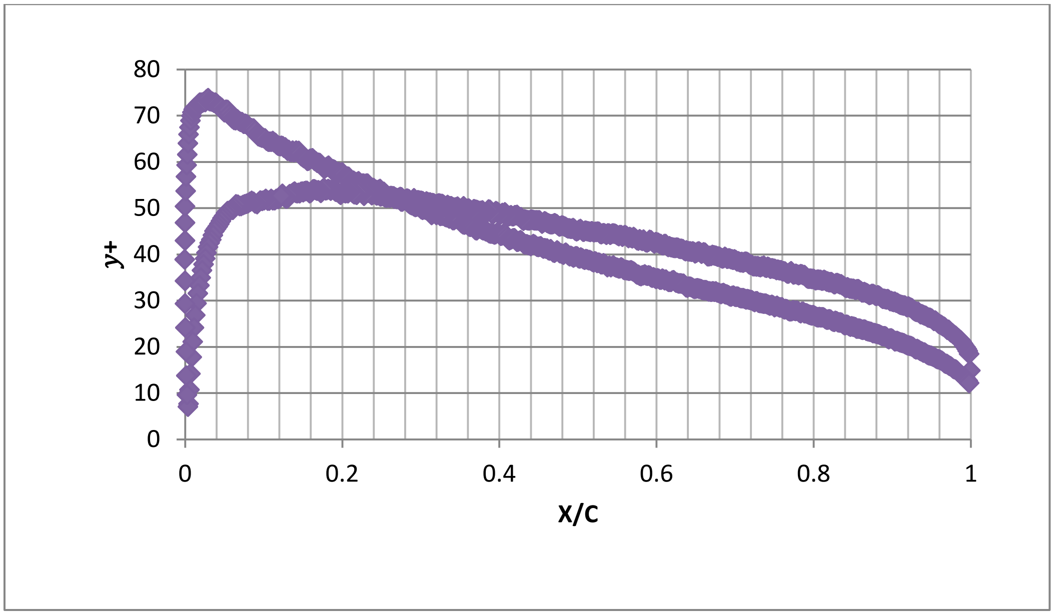

Figure 4.1. y^+ calculation

4.3. Periodic Convergence

In order to estimate C_p it is necessary to consider the periodic convergence. Figure 4.2 illustrates the C_p convergence results of 2D fine mesh with respect to time for $\lambda = 1$. It should be stated that the value of C_p demonstrates a transient behavior before reaching a periodic pattern. As it can be seen, after the $T = 2\ (Sec)$ the results demonstrate a periodic behavior. At this stage the average calculated $C_p = 0.1083$. It should be mentioned that the calculations are based on the total torque of the four blades.

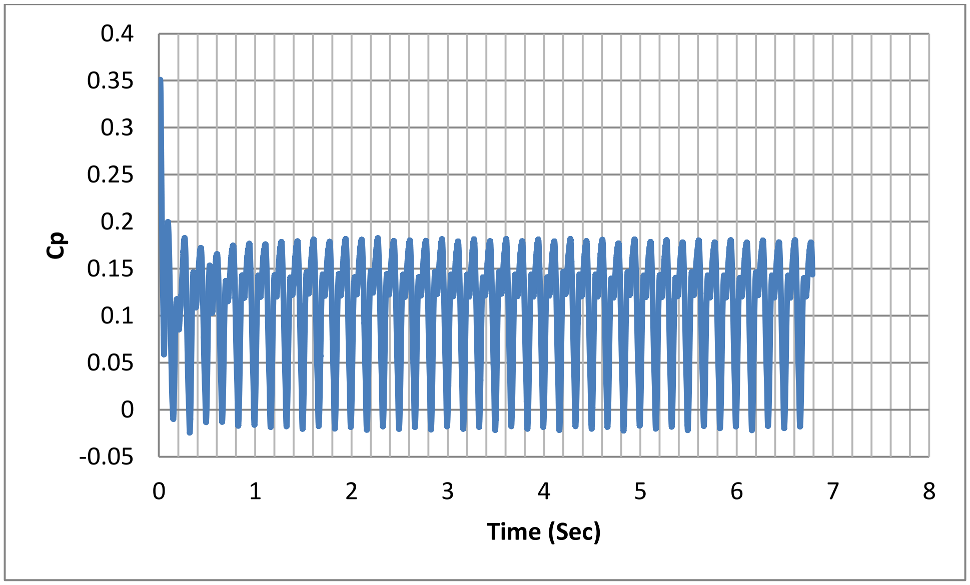

Figure 4.2. C_p versus time for $\lambda = 1$ (2D fine mesh)

Figure 4.3 depicts the variation of C_p for the 2D fine mesh with respect to time at $\lambda = 2$. The obtained results shows that the periodic pattern is observed around $T = 6\ (Sec)$. The averaged calculated C_p for the last two cycles after observing the convergence is $C_p = 0.3168$.

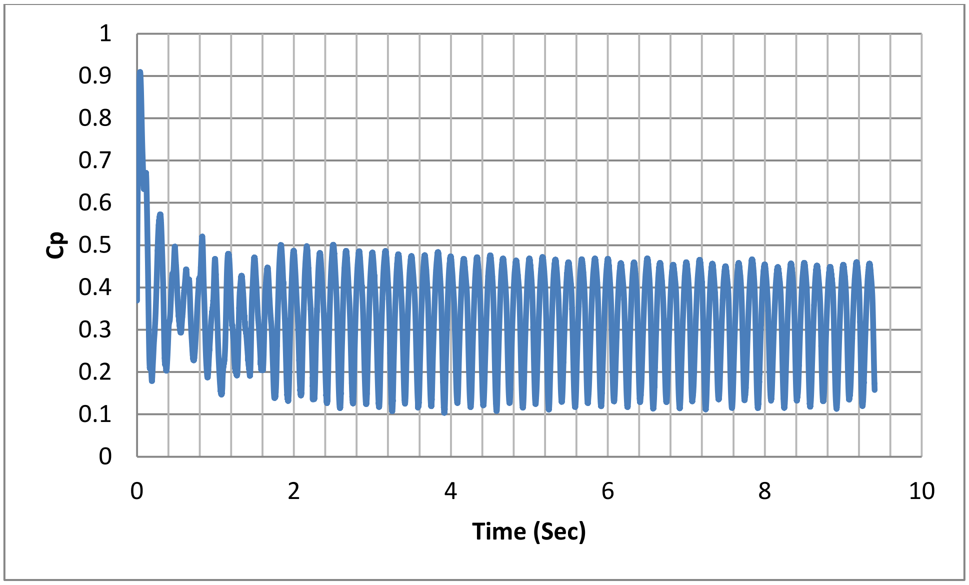

Figure 4.3. C_p versus time for $\lambda = 2$ (2D fine mesh)

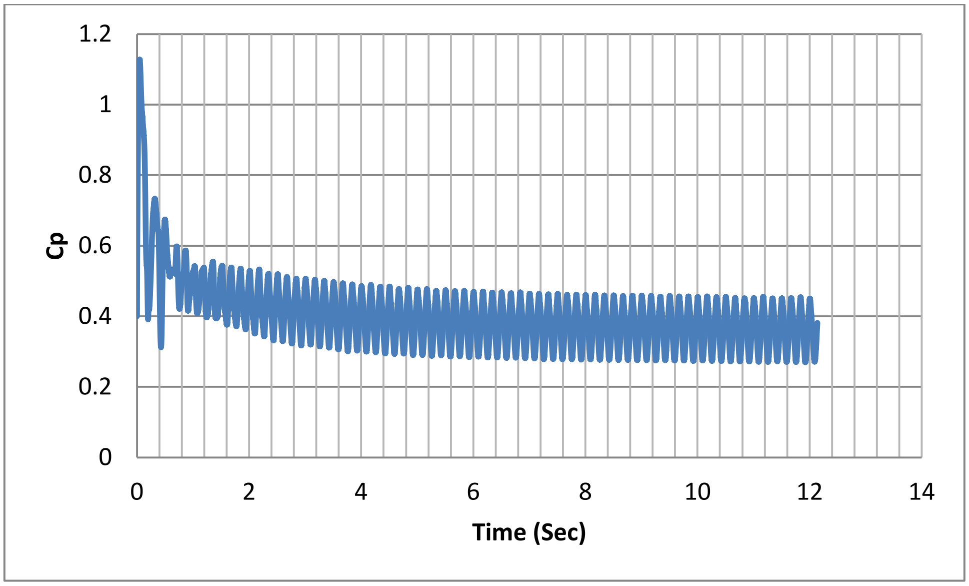

Figure 4.4. C_p versus time for $\lambda = 2.4$ (2D fine mesh)

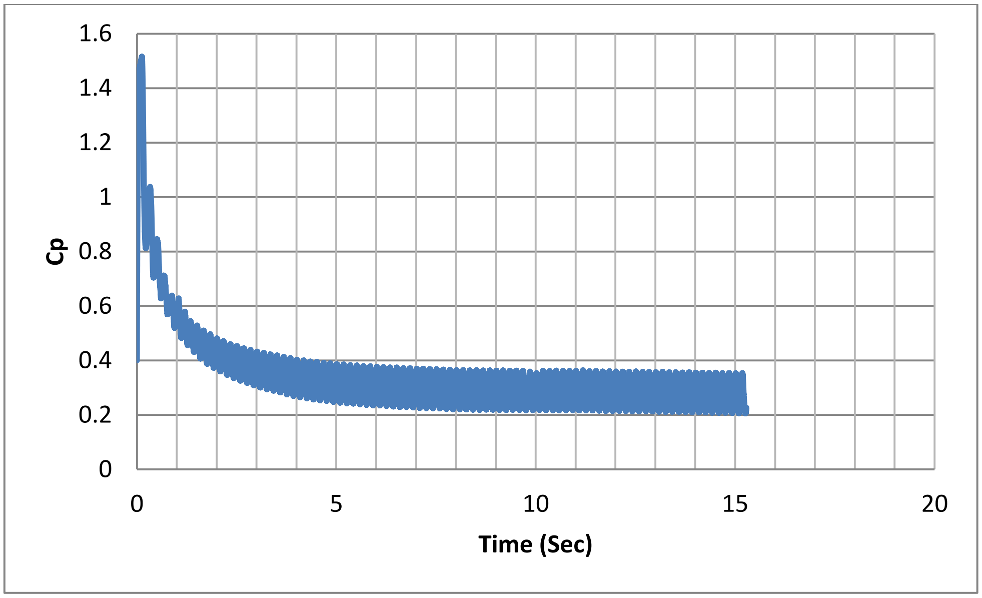

Figure 4.5. C_p versus time for $\lambda = 3$ (2D fine mesh)

Figure 4.4 and Figure 4.5 show the variation of C_p with respect to time at $\lambda = 2.4$ & $\lambda = 3$ for the 2D fine mesh. The obtained results shows that the converged periodic oscillation starts around $T = 9\ (Sec)$ and $T = 10\ (Sec)$ and the averaged obtained C_p for the last two cycles, after observing the convergence, are $C_p = 0.3614$ and $C_p = 0.2852$, respectively.

On the other hand, Figure 4.6 shows the C_p curve over time for the 3D analysis at $\lambda = 2$. Similarly, the value of C_p follows a transient behavior before reaching a periodic convergence. Based on the last two cycles, the averaged power coefficient, obtained in this 3D investigation, is $C_p = 0.178$. Furthermore, it can be clearly seen that for the last two cycles the convergence pattern started earlier compared to the 2D results at $\lambda = 2$

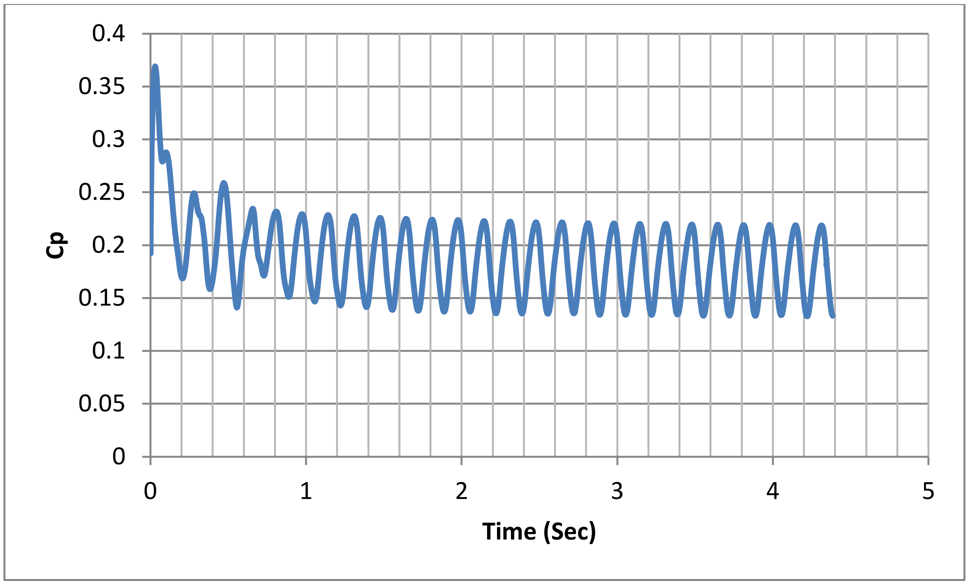

Figure 4.6. C_p versus time for $\lambda = 2$ (3D mesh)

4.4. Time-step Analysis

In transient simulations, a simple-based solver allows large time-step marching and time-step can be chosen as fixed or adjustable. In this study, adjustable time-step is selected, that is based on the maximum Courant (CFL) number. It should be noted that for the very large CFL numbers, the system might become unstable. Therefore, the maximum CFL number, employed in this numerical study, is $(CFL = 15)$, which is equivalent to an average value of time-step ≈ 0.0003 per iteration.

4.5. Effect of Mesh Density on C_p Convergence

Figure 4.7 illustrates the variation of C_p for the 2D coarse, medium and fine meshes at $\lambda = 3$. It can be clearly seen that as the mesh resolution is improved, the numerical error is decreased. Besides, the amplitude of C_p curves is demonstrating the same oscillatory behavior by reaching convergence. The averaged calculated C_p at $\lambda = 3$ for the coarse, Medium and fine meshes are $C_p = 0.2527$, $C_p = 0.2796$ and $C_p = 0.2809$, respectively.

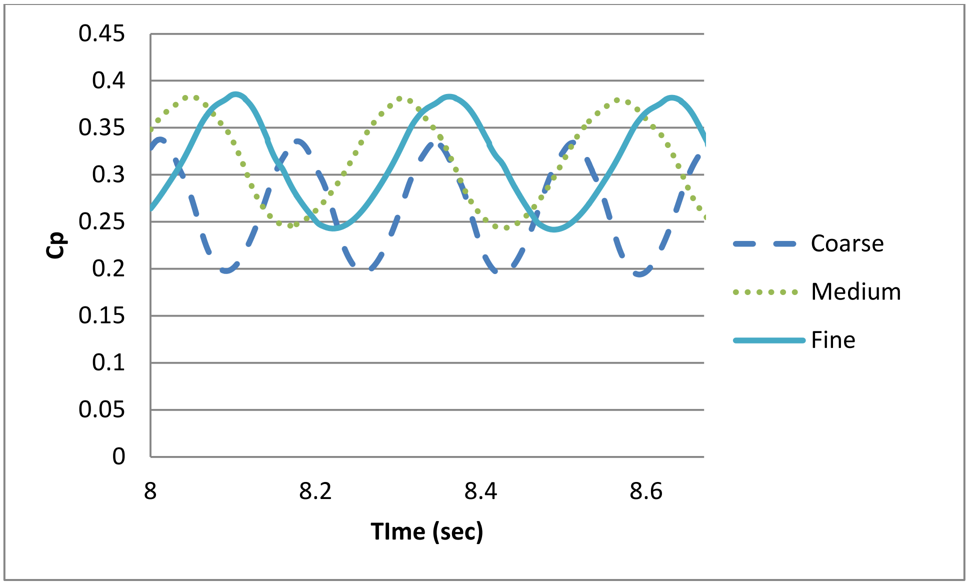

Figure 4.7. C_p for coarse, medium and fine mesh at $\lambda = 3$

4.6. Validation

Figure 4.8 illustrates the validation of the numerical results for three meshes with experimental data, quantitatively. For all three grids the maximum power coefficients are obtained at $\lambda = 2.4$. However, simulations on coarse mesh predicted lower C_p compared to medium and fine cases. In contrast, results from medium and fine grids are in a perfect fit. All the three numerical results of the 2D mesh demonstrated higher $C_p$values compared to the experimental data. The discrepancies lie on the existence of the rotor hub and blades connections that result in reducing the C_p of real turbine by affecting the flow turbulence features around the blades. In addition, tip vortex and other 3D turbulence features influence the aerodynamics forces of the blades.

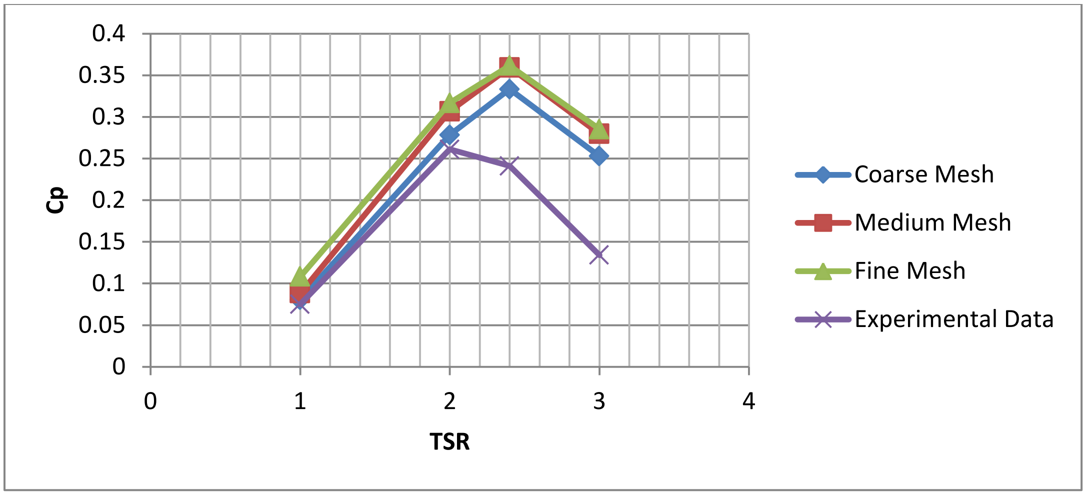

Figure 4.8. Comparison of CFD and experimental results

The values of the numerical techniques and experimental results are also reported in Table 4.2. In 2001, performance data was collected for a single turbine located in Palm Spring. The daily electrical output and average wind speed were recorded and used in the calculation of the coefficient of power. The electric output was converted into the shaft output by using an estimated power train efficiency of 0.92 and an estimated gearbox efficiency of 0.9325.

Table 4.2. CFD and experimental comparison of C_p

TSR	**Coarse Mesh**	**Medium Mesh**	**Fine Mesh**	**Experimental Data**
1	0.0805	0.0883	0.1083	0.075
2	0.2784	0.3067	0.3168	0.261
2.4	0.3332	0.3594	0.3614	0.241
3	0.2527	0.2796	0.2852	0.134

5. 2D Results and Discussion

In this chapter

The velocity and vorticity structures as well as the variation of torque against azimuthal angle, for the 2D mesh, at different TSRs, are presented.

5.1. 2D Results of Velocity Field

5.1.1. Velocity Field at $\lambda = 3$

As it was previously discussed, the flow analysis is performed at different TSRs. Figure 5.1 shows the major concentration of the results in which the separation and vortex shedding occurred, i.e., $\psi = 90^{\circ}$ up to $\psi = 180^{\circ}$. Figures 5.2 to 5.5 depict the instantaneous velocity magnitude at $\psi = 90, 120, 150\ and\ 180$ degrees at $\lambda = 3$, respectively. The fluid flows from left to right and the turbine moves anti-clockwise. Figure 5.2 shows the stagnation point at the suction surface of the blade at $\psi = 90^{\circ}$. It can be clearly seen that low velocity region is achieved inside and downstream of the turbine. Moreover, at $\psi = 90^{\circ}$, the high velocity region is visualized at the leading edge and lower surface of the blade. Figure 5.3 illustrates the low pressure region at the leading edge as well as the trailing vortex of the blade at $\psi = 120^{\circ}$.

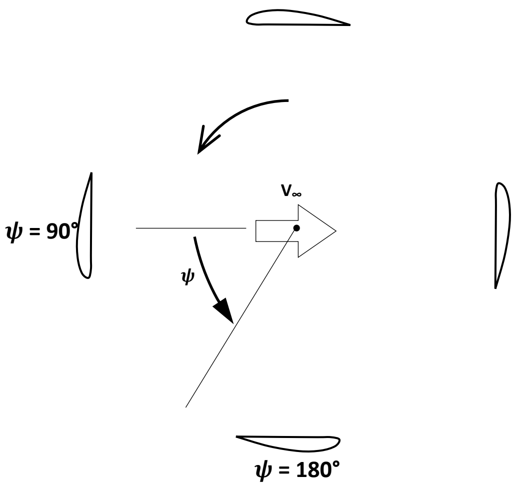

Figure 5.1. Region of separation and vortex shedding

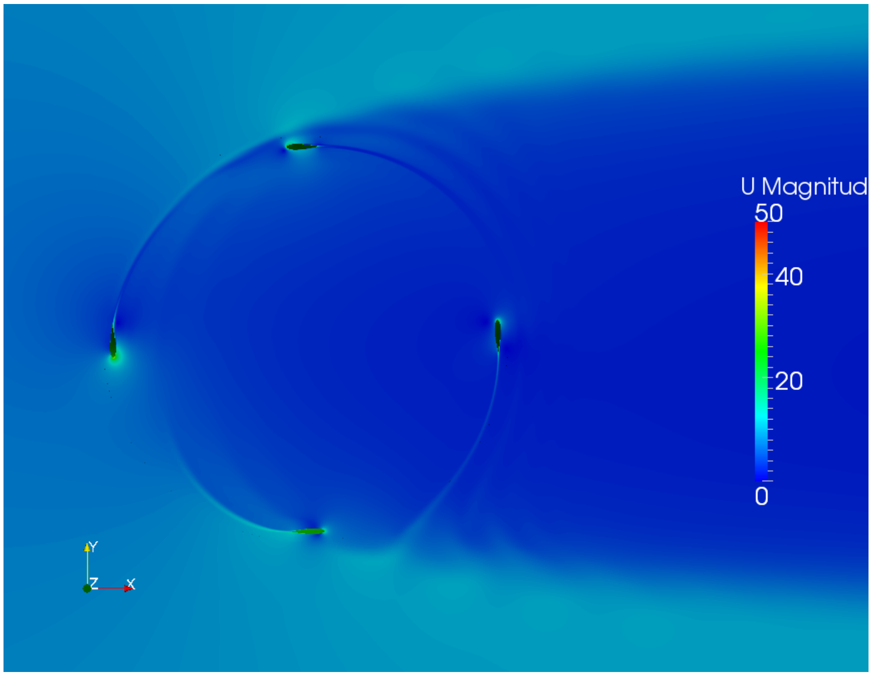

Figure 5.2. Velocity magnitude (m/s) at $\lambda = 3$ and $\psi = 90^{\circ}$

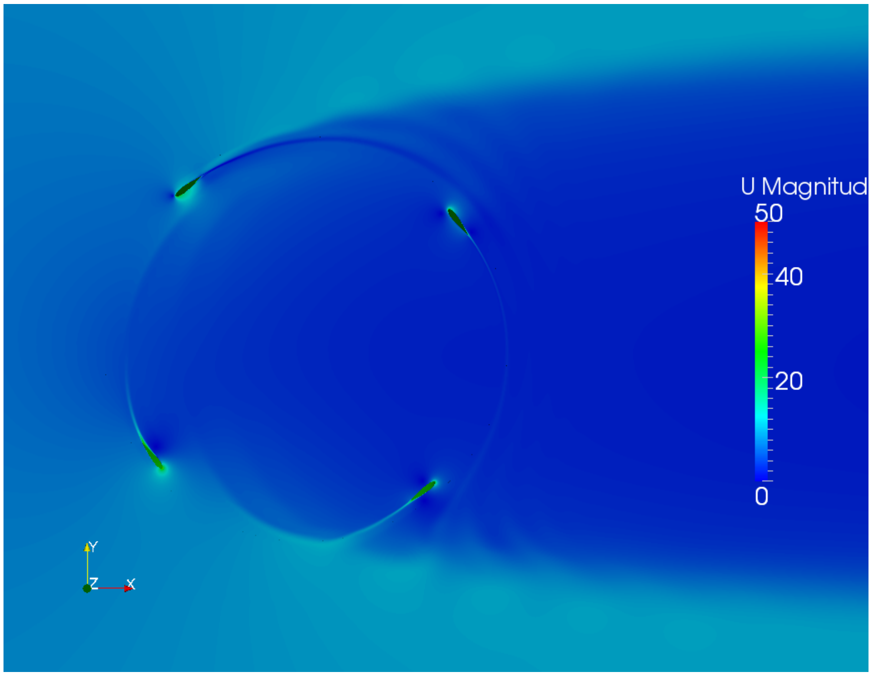

Figure 5.3. Velocity magnitude (m/s) at $\lambda = 3$ and $\psi = 120^{\circ}$

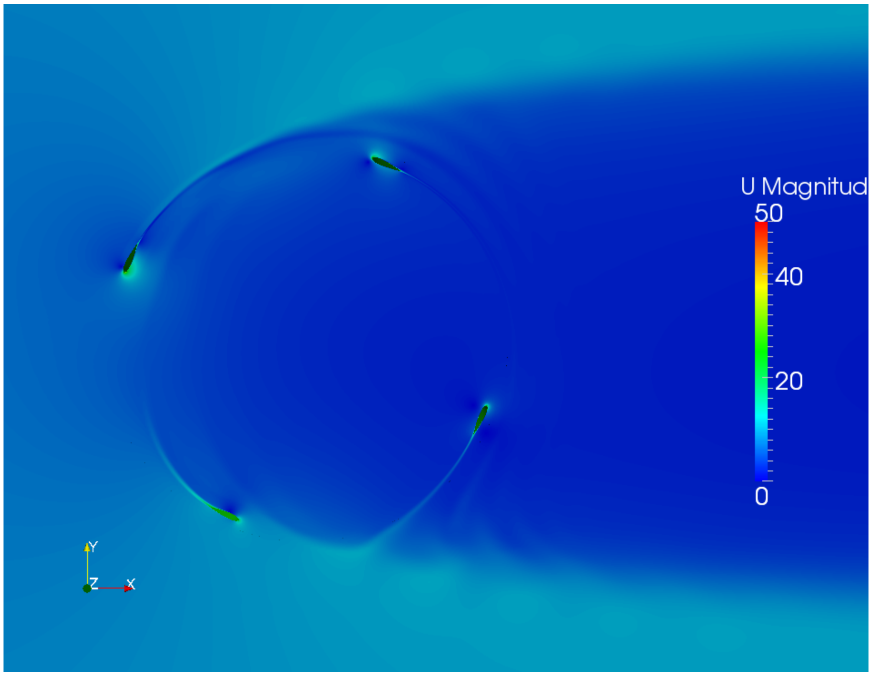

Figure 5.4. Velocity magnitude (m/s) at $\lambda = 3$ and $\psi = 150^{\circ}$

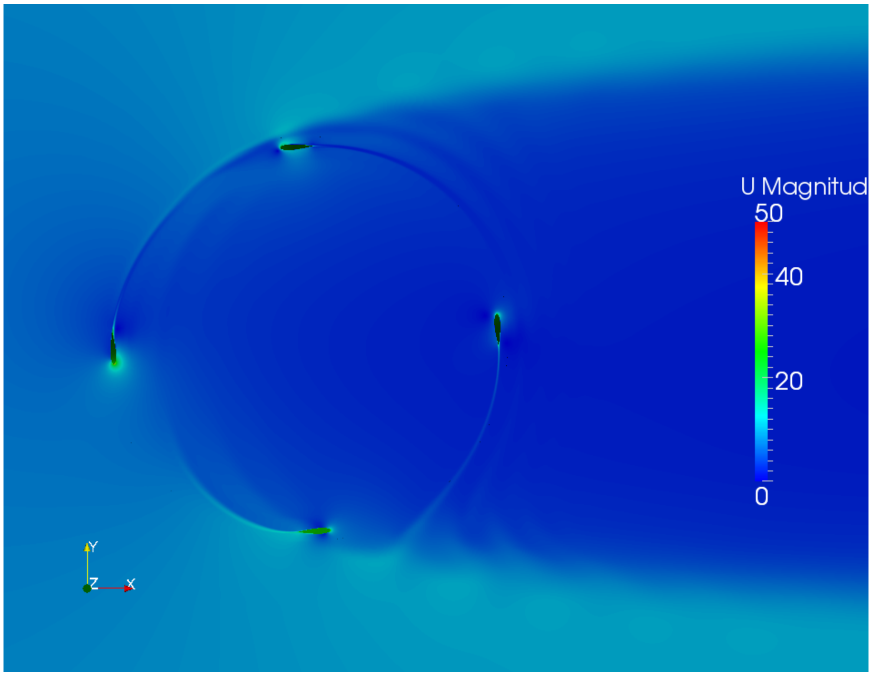

Figure 5.5. Velocity magnitude (m/s) at $\lambda = 3$ and $\psi = 180^{\circ}$

Low velocity region is observed at the pressure surface of the blade at $\psi = 150^{\circ}$, Figure 5.4. As the blade rotates to $\psi = 180^{\circ}$, Figure 5.5, low velocity and stagnation regions are seen at both the pressure and suction surface of airfoil.

5.1.2. Velocity Field at $\lambda = 2.4$

The instantaneous velocity contours at $\psi = 90, 120, 150$ *and* 180 degrees are shown in Figures 5.6 to 5.9, respectively. The maximum velocity values are obtained around the leading edge of the blade at $\psi = 90^{\circ}$, Figure 5.6, whereas from the trailing edge up to the middle of the blade upper surface, velocity is almost zero. As the azimuthal angle increases from $\psi = 90^{\circ}$ to $\psi = 120^{\circ}$, the stagnation point is moved towards the aft of the suction surface, Figure 5.7. It can also be clearly seen that the high velocity region is formed around the lower surface towards the trailing edge.

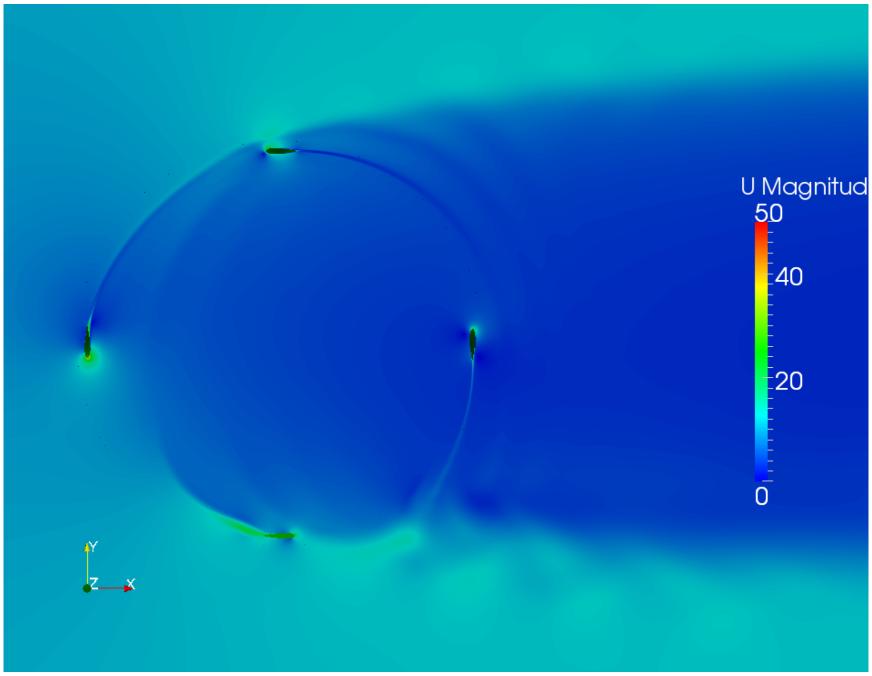

Figure 5.6. Velocity magnitude (m/s) at $\lambda = 2.4$ and $\psi = 90^{\circ}$

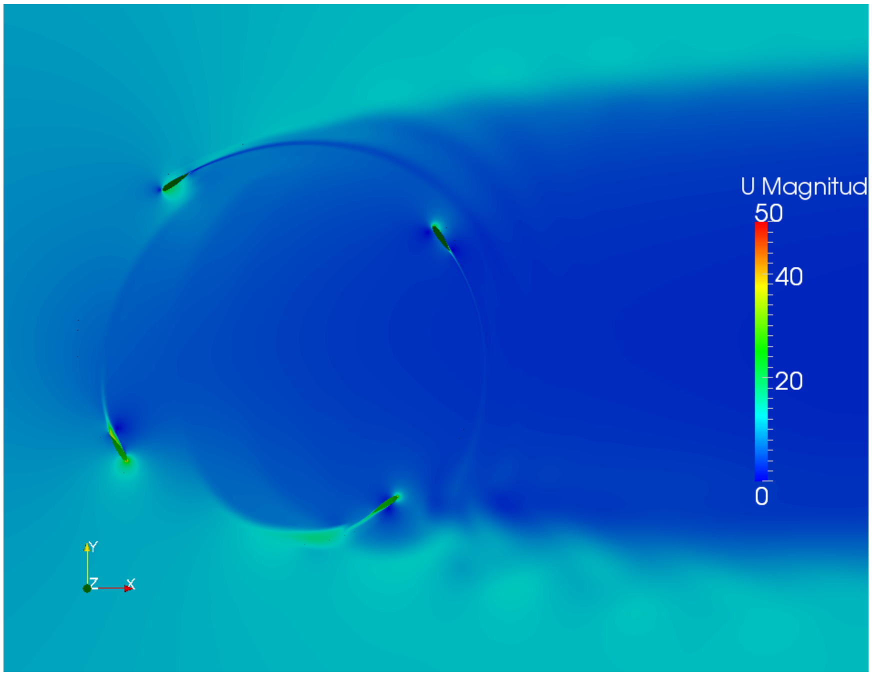

Figure 5.7. Velocity magnitude (m/s) at $\lambda = 2.4$ and $\psi = 120^{\circ}$

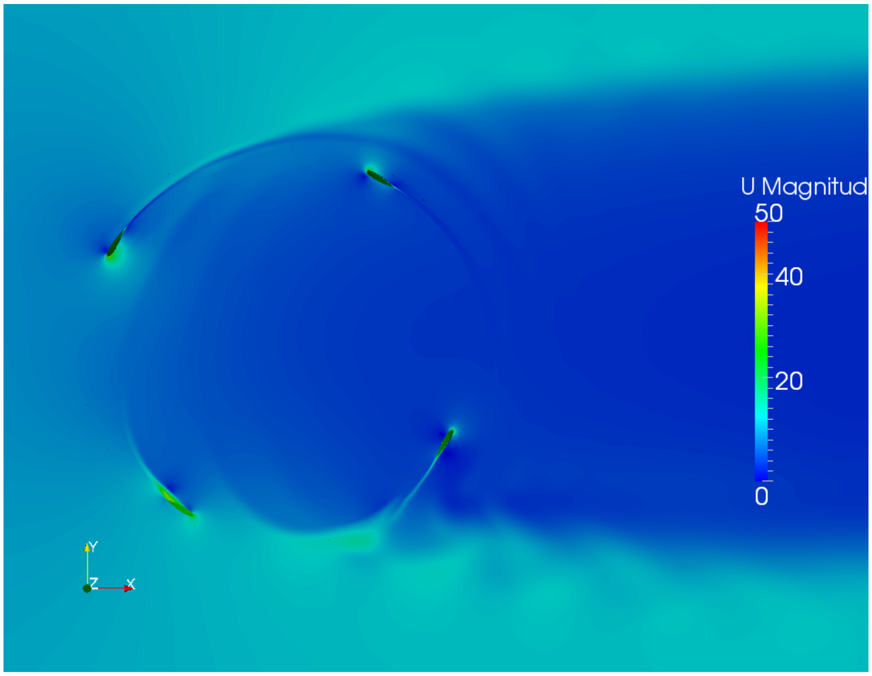

Figure 5.8. Velocity magnitude (m/s) at $\lambda = 2.4$ and $\psi = 150^{\circ}$

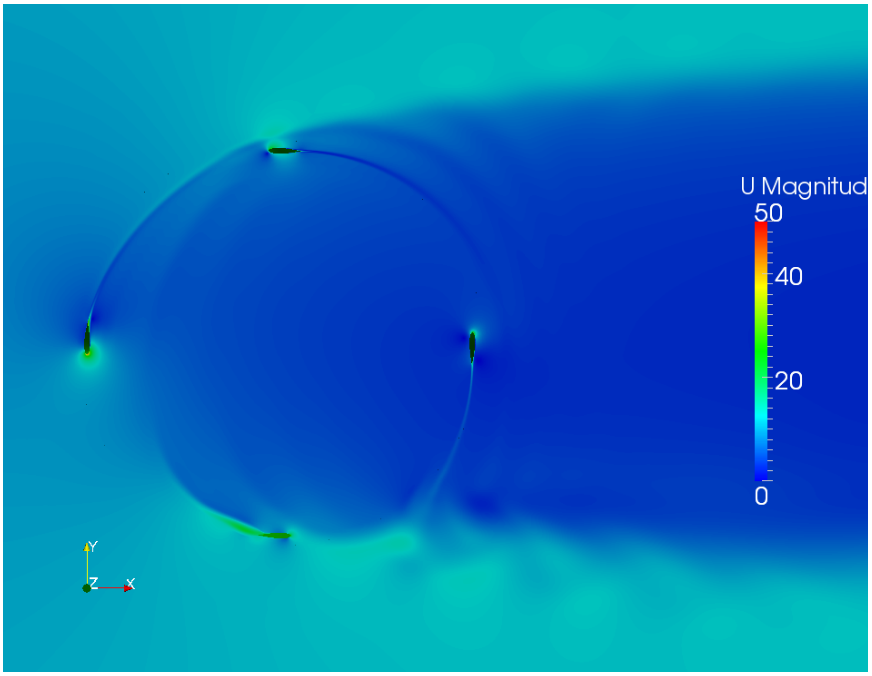

Figure 5.9. Velocity magnitude (m/s) at $\lambda = 2.4$ and $\psi = 180^{\circ}$

As the flow encounters the upper surface of the blade low velocity region and stagnation point are observed, Figure 5.8. At $\psi = 180^{\circ}$, Figure 5.9, the separation point is moved further towards the trailing edge.

5.1.3. Velocity Field at $\boldsymbol{\lambda = 2}$

Figures 5.10 to 5.13 show the instantaneous velocity magnitude at $\psi = 90, 120, 150$ *and* 180 degrees at $\lambda = 2$, respectively. The upstream of the turbine is where, the fluid flows and as soon as the flow passes the counter-clockwise rotating turbine, it leaves the domain. Similarly, the stagnation point is observed at the suction surface of the airfoil at $\psi = 90^{\circ}$, Figure 5.10.

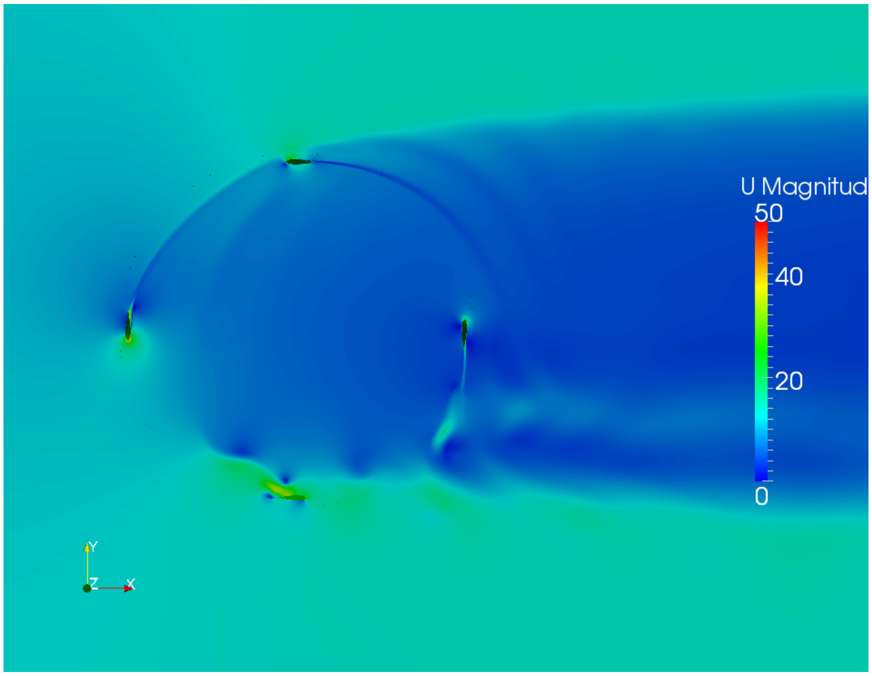

Figure 5.10. Velocity magnitude (m/s) at $\lambda = 2$ and $\psi = 90^{\circ}$

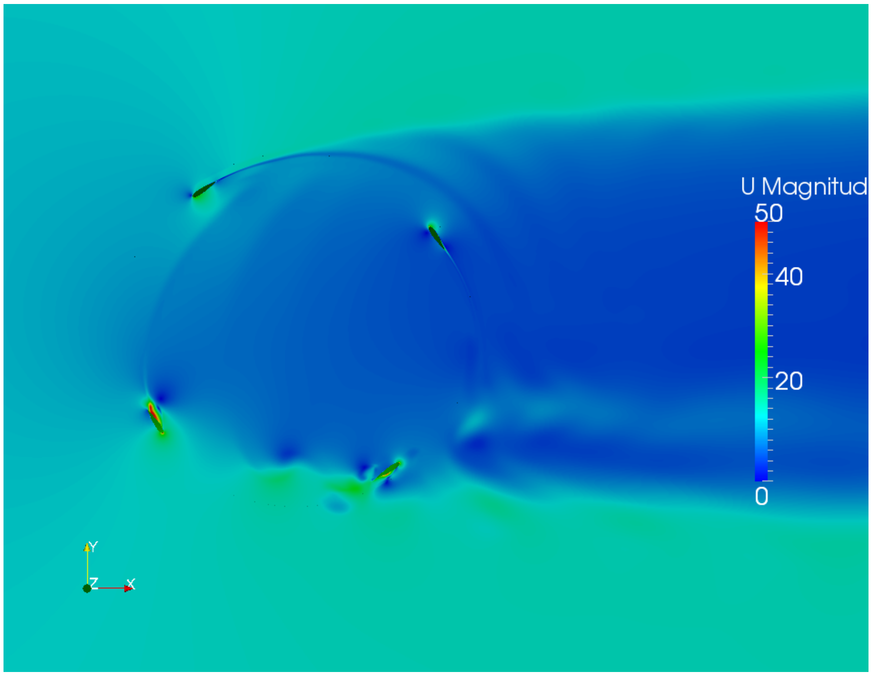

Figure 5.11. Velocity magnitude (m/s) at $\lambda = 2$ and $\psi = 120^{\circ}$

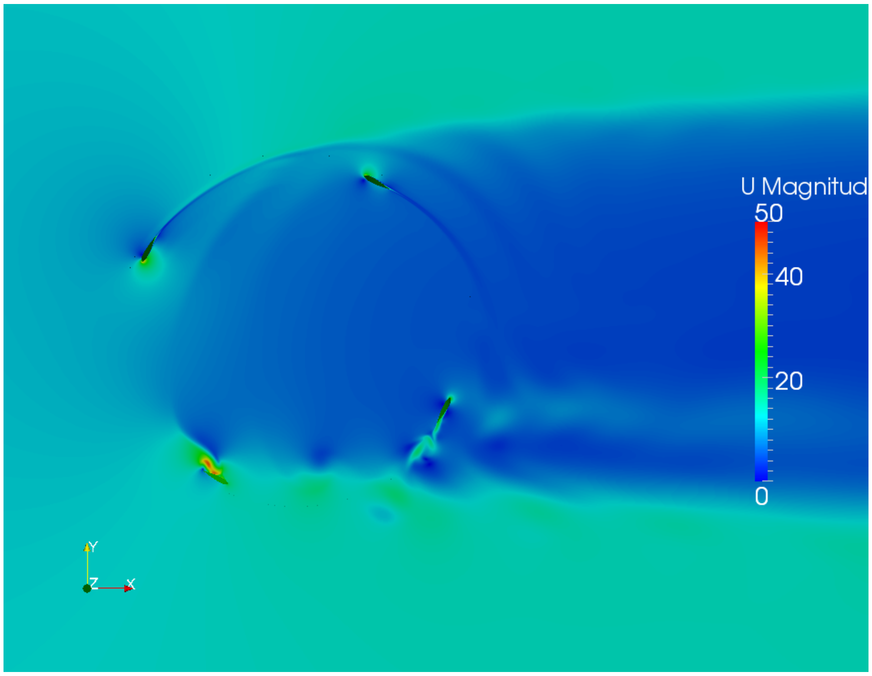

Figure 5.12. Velocity magnitude (m/s) at $\lambda = 2$ and $\psi = 150^{\circ}$

Furthermore, at $\psi = 90^{\circ}$, the high velocity region is visualized at the leading edge of the blade. Figure 5.11 depicts the change of location of the stagnation point towards the trailing edge of the airfoil at $\psi = 120^{\circ}$, where, the high velocity region is seen in the pressure surface. The separation point is closed to the airfoil trailing edge at $\psi = 150^{\circ}$, Figure 5.12, where, the high pressure region is visualized at trailing edge of the airfoil. As the blade rotates to $\psi = 180^{\circ}$, Figure 5.13, high velocity region is seen at the airfoil pressure surface, where, the maximum drag is achieved.

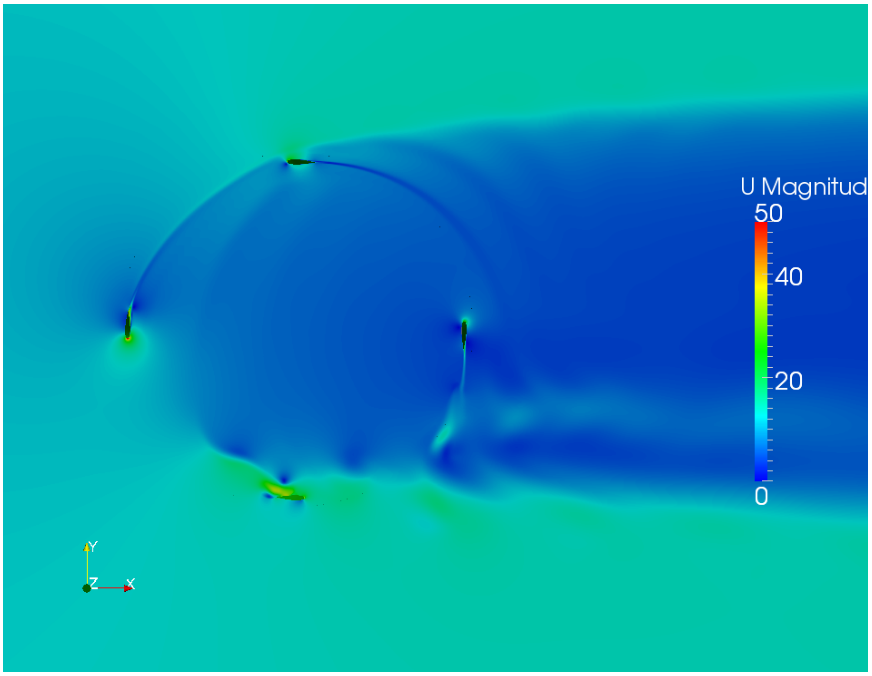

Figure 5.13. Velocity magnitude (m/s) at $\lambda = 2$ and $\psi = 180^{\circ}$

5.1.4. Velocity Field at $\lambda = 1$

Figures 5.14 to 5.17 illustrate the instantaneous velocity field for the blades at $\psi = 60, 90, 120\ and\ 150$ degrees, respectively. It should be mentioned that in the case of $\lambda = 1$, to allow for maximum coverage of the flow features, e.g., dynamic stall, results are visualized from 60 to 150 degrees. Figure 5.14 shows the location of stagnation point at the upper surface of the airfoil. Furthermore, high velocity region is observed around the airfoil leading edge, at $\psi = 60^{\circ}$. At $\psi = 90^{\circ}$, low pressure region is observed near the trailing edge of the blade, Figure 5.15. It can also be seen that the stagnation point is moved towards the middle of the upper surface of the airfoil.

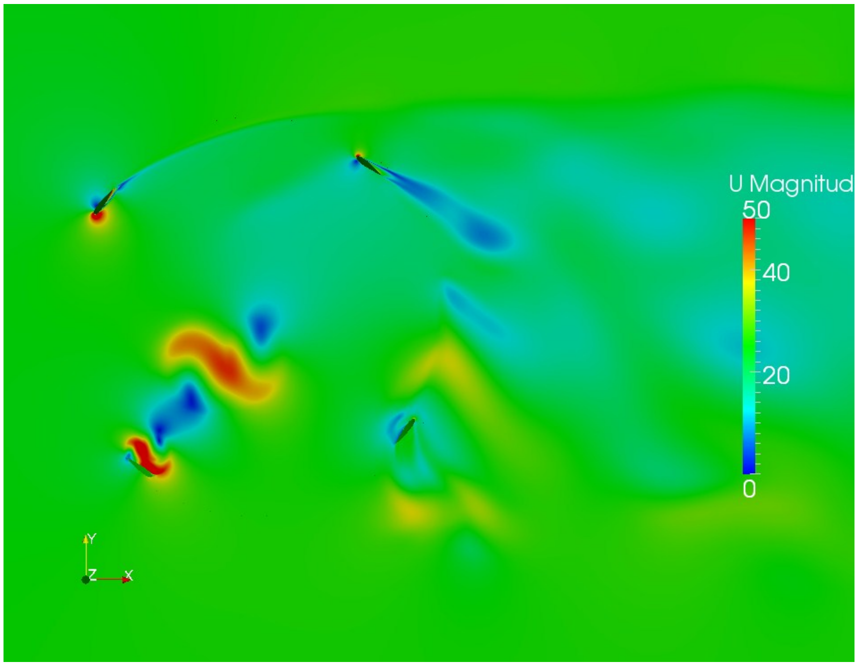

Figure 5.14. Velocity magnitude (m/s) at $\lambda = 1$ and $\psi = 60^{\circ}$

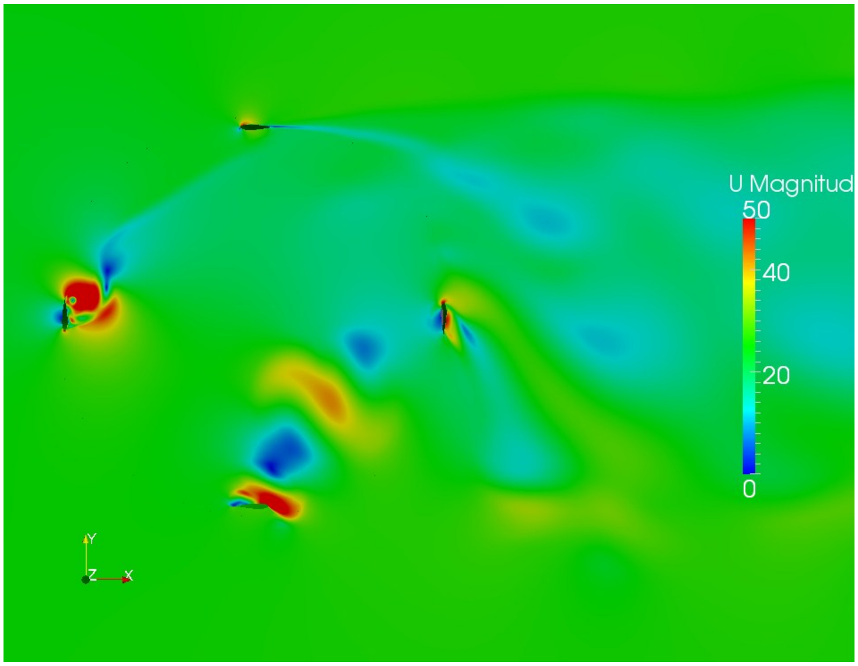

Figure 5.15. Velocity magnitude (m/s) at $\lambda = 1$ and $\psi = 90^{\circ}$

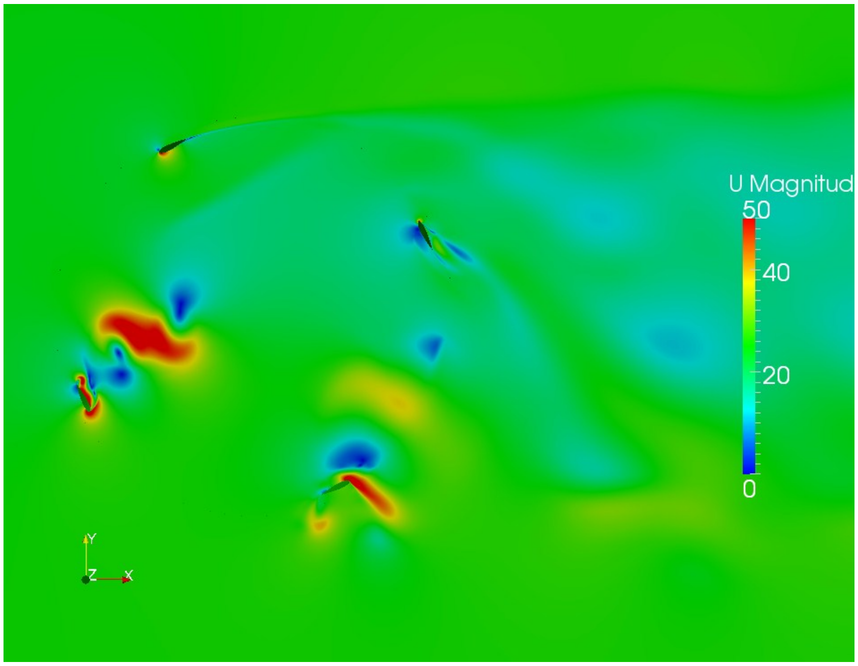

Figure 5.16. Velocity magnitude (m/s) at $\lambda = 1$ and $\psi = 120^{\circ}$

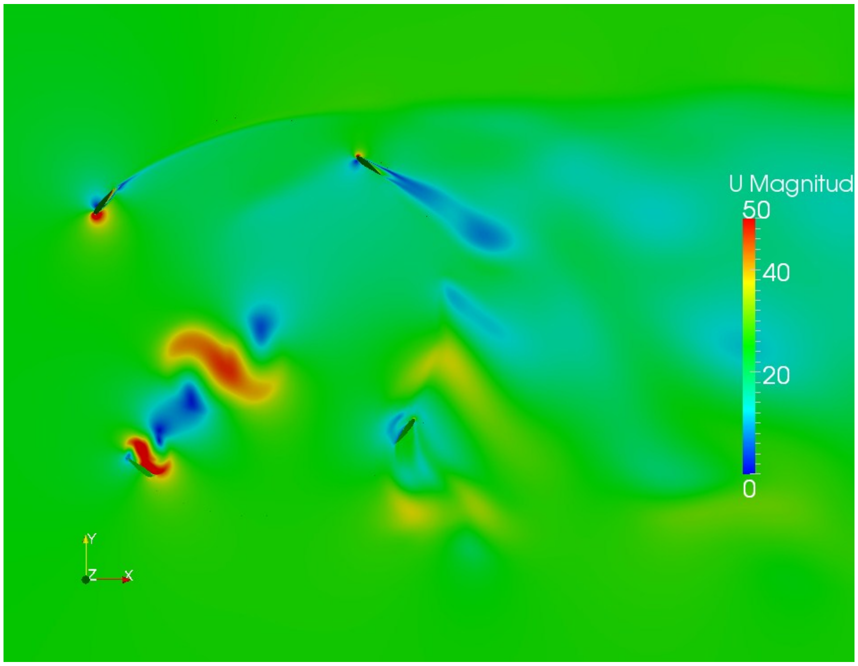

Figure 5.17. Velocity magnitude (m/s) at $\lambda = 1$ and $\psi = 150^{\circ}$

High velocity region is visualized at the leading edge and lower surface of the airfoil at $\psi = 120^{\circ}$, Figure 5.16. The separation point is moved further towards the trailing edge at $\psi = 150^{\circ}$, Figure 5.17, where, the low pressure region is visualized in the lower surface of the airfoil. Moreover, at $\psi = 150^{\circ}$, stagnation point is seen at the trailing edge of the blade.

5.2. 2D Results of Vorticity Structure

5.2.1. Vorticity Structure at $\boldsymbol{\lambda = 3}$

Figures 5.18 to 5.21 demonstrate the vorticity contours at different azimuthal angle at $\lambda = 3$. Figure 5.18 shows the negative and positive vortices on the upper and lower surface of the blade, respectively. It can be visualized that the clockwise vortex shedding are leaving the turbine and dissipating in the downstream flow at $\psi = 90^{\circ}$. As the blade turns 30 more degrees in counter-clockwise direction, the generated vortices are interacted with the previous adjacent blade, Figure 5.19. At $\psi = 150^{\circ}$, the positive vortex flow tends to detach from the blade as it started developing from the pressure surface of the airfoil, Figure 5.20. Moreover, both the positive and negative vortices are captured closed to the trailing edge of the blade, Figure 5.21, and the previously generated anti-clockwise vortices hit the associated blade.

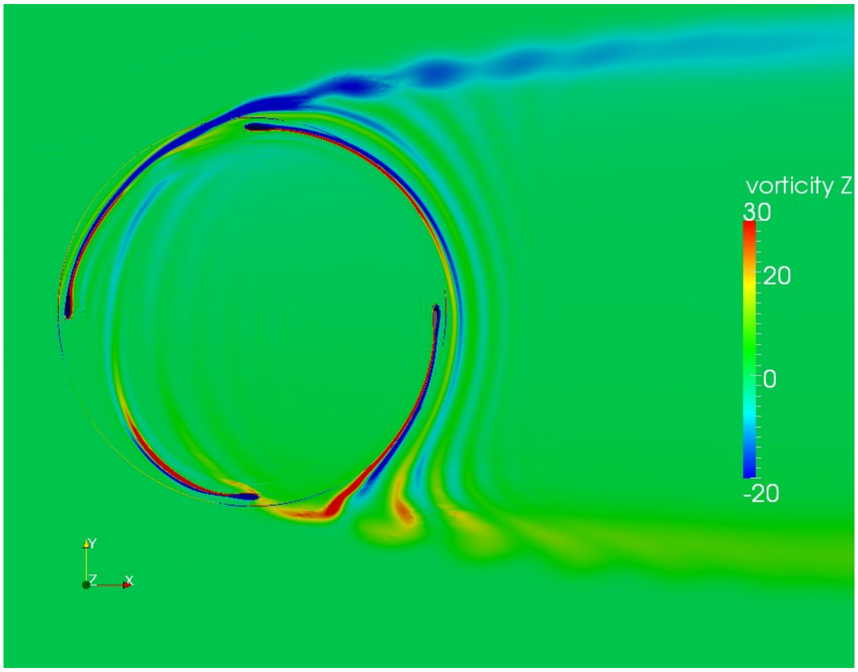

Figure 5.18. Vorticity $(1/s)$ contour at $\lambda = 3$ and $\psi = 90^{\circ}$

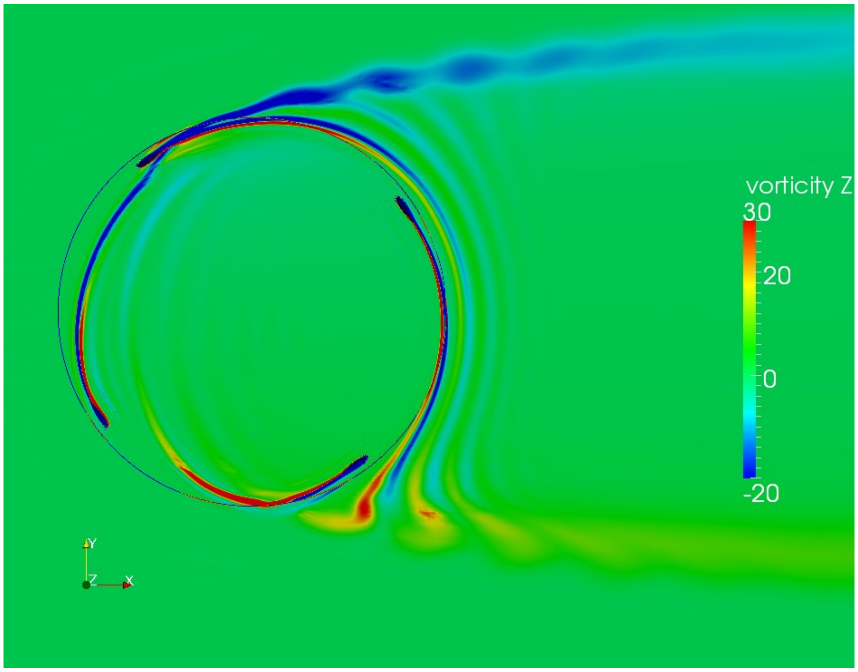

Figure 5.19. Vorticity $(1/s)$ contour at $\lambda = 3$ and $\psi = 120^{\circ}$

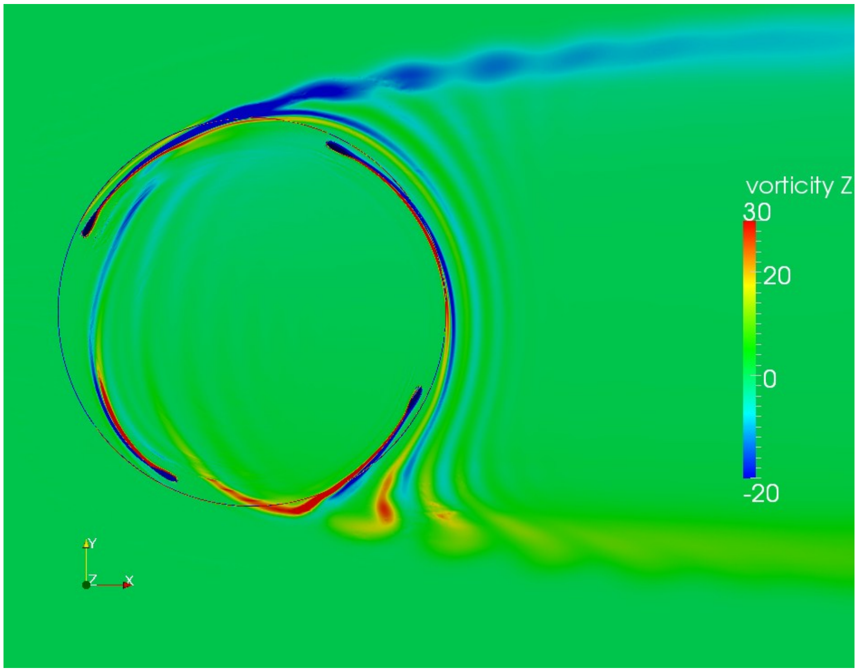

Figure 5.20. Vorticity $(1/s)$ contour at $\lambda = 3$ and $\psi = 150^{\circ}$

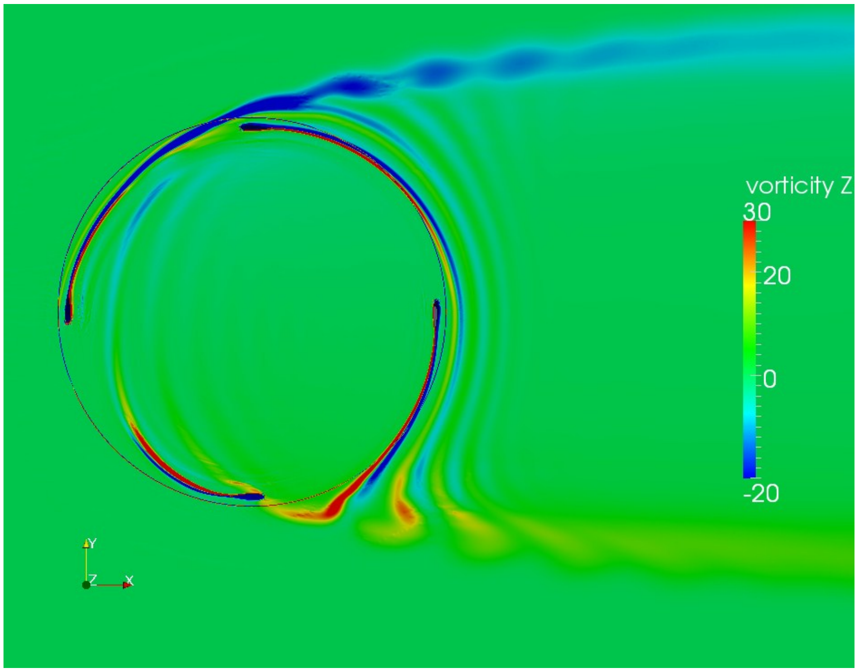

Figure 5.21. Vorticity $(1/s)$ contour at $\lambda = 3$ and $\psi = 180^{\circ}$

5.2.2. Vorticity Structure at $\boldsymbol{\lambda = 2.4}$

Figures 5.22 to 5.25 demonstrate the vorticity contours at various azimuthal angles at $\lambda = 2.4$. Figure 5.22 depicts the clockwise and counter-clock-wise vortices in top and bottom of the blade at $\psi = 90^{\circ}$, respectively. It also shows that the generated vortices travelled towards the previous adjacent blade. Figure 5.23 shows that the previous adjacent blade hit the generated negative vortices at $\psi = 120^{\circ}$. Furthermore, the gradual dissipation of the negative vortex into the main flow can be visualized.

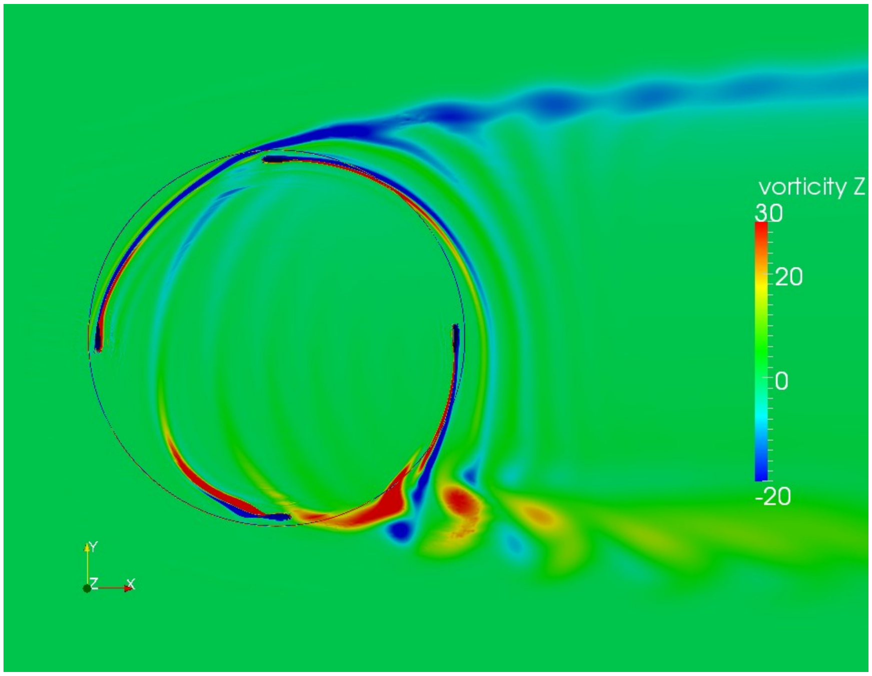

Figure 5.22. Vorticity $(1/s)$ contour at $\lambda = 2.4$ and $\psi = 90^{\circ}$

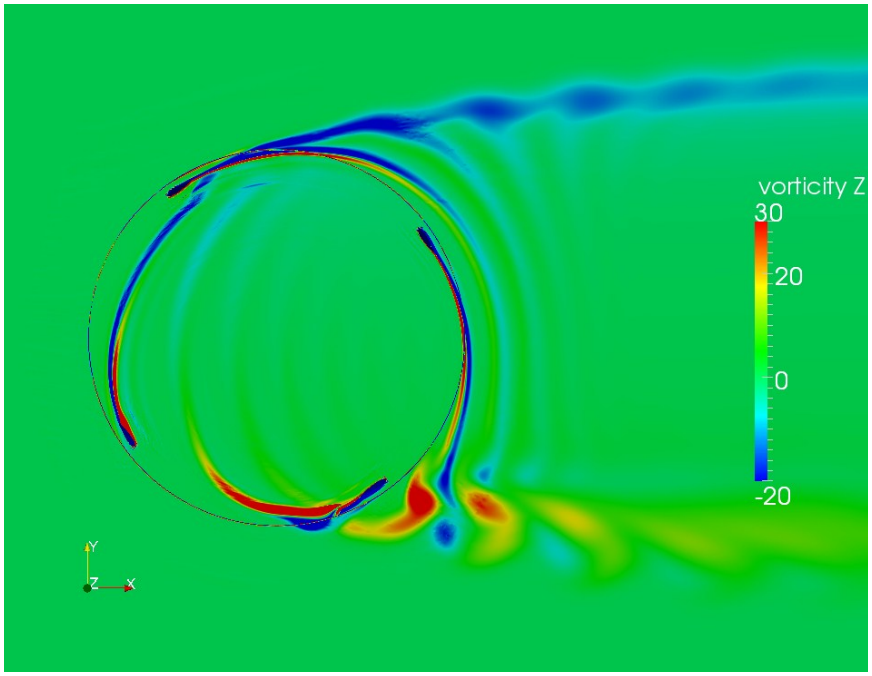

Figure 5.23. Vorticity $(1/s)$ contour at $\lambda = 2.4$ and $\psi = 120^{\circ}$

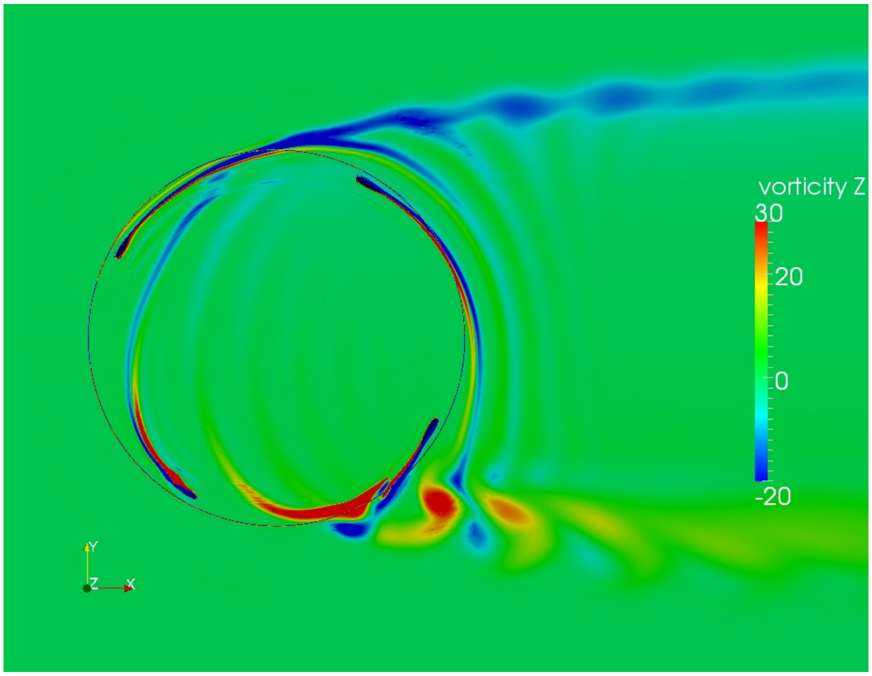

Figure 5.24. Vorticity $(1/s)$ contour at $\lambda = 2.4$ and $\psi = 150^{\circ}$

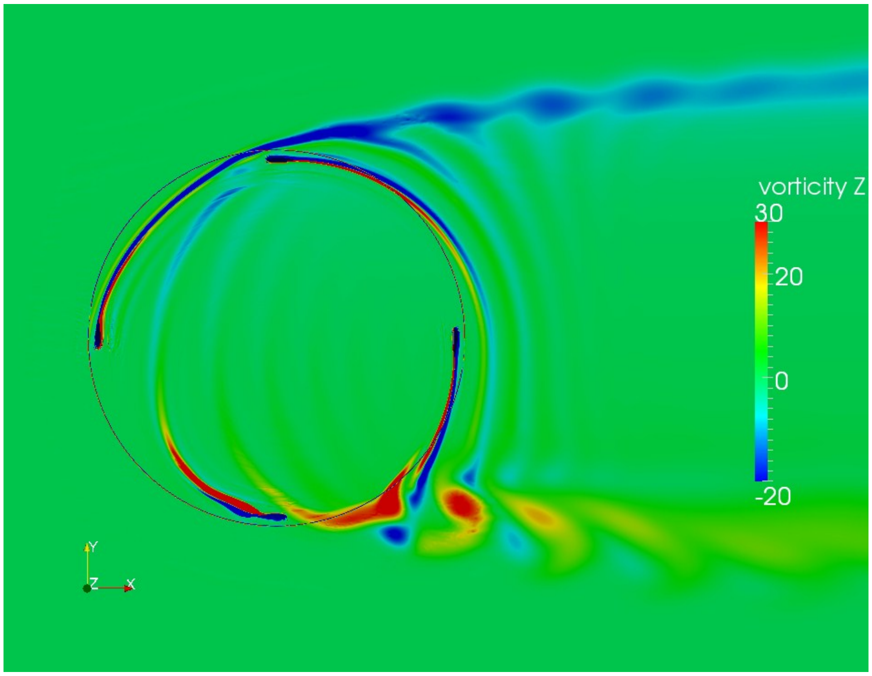

Figure 5.25. Vorticity $(1/s)$ contour at $\lambda = 2.4$ and $\psi = 180^{\circ}$

Figure 5.24 shows that the positive vortex is surrounded by two clockwise vortices. The separation and dissipation of the negative vortex structure from the blade is observed at $\psi = 180^{\circ}$, Figure 5.25, where, the positive vortex tends to detach from the airfoil.

5.2.3. Vorticity Structure at $\lambda = 2$

Figures 5.26 to 5.29 show the vorticity structures at various blade locations at $\lambda = 2$. Figure 5.26 depicts the attachment of clockwise and counter-clockwise vortices to the top and bottom of the airfoil, respectively. At $\psi = 90^{\circ}$, the flow is separated and the counter-rotating vortex starts developing from the pressure surface of the airfoil. Moreover, it is seen that the previous adjacent blade encounters the negative vortices. Figure 5.27 shows the gradual dissipation of the clockwise vortex at $\psi = 120^{\circ}$ as well as the strong presence of positive vortex at the lower surface of the airfoil. It can also be seen that the separated vortices bounced the next adjacent airfoil.

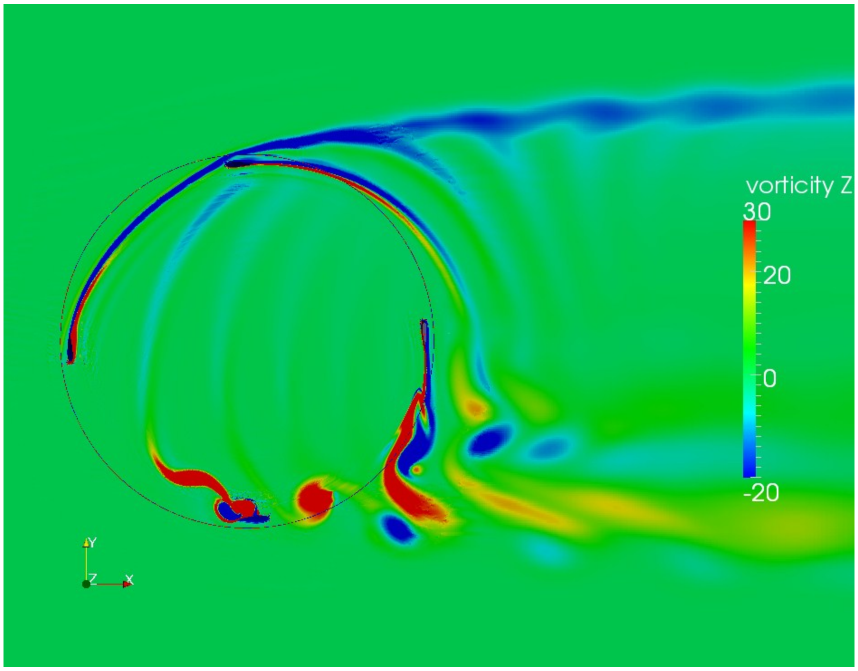

Figure 5.26. Vorticity $(1/s)$ contour at $\lambda = 2$ and $\psi = 90^{\circ}$

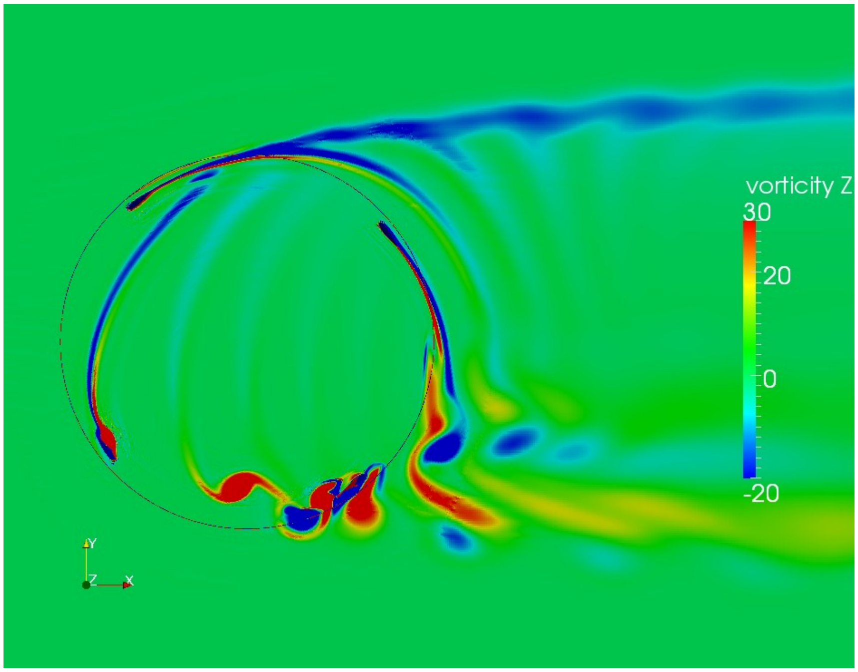

Figure 5.27. Vorticity $(1/s)$ contour at $\lambda = 2$ and $\psi = 120^{\circ}$

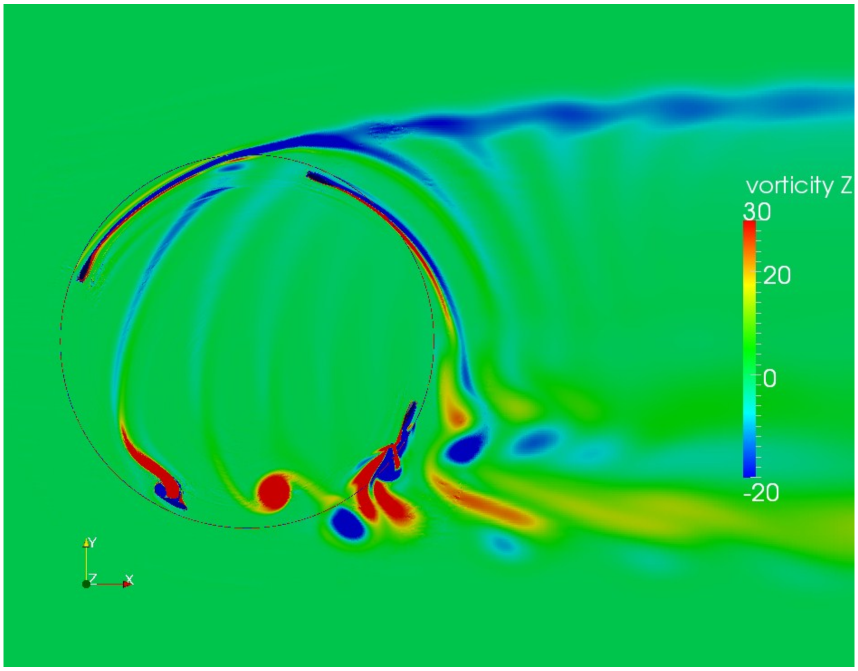

Figure 5.28. Vorticity $(1/s)$ contour at $\lambda = 2$ and $\psi = 150^{\circ}$

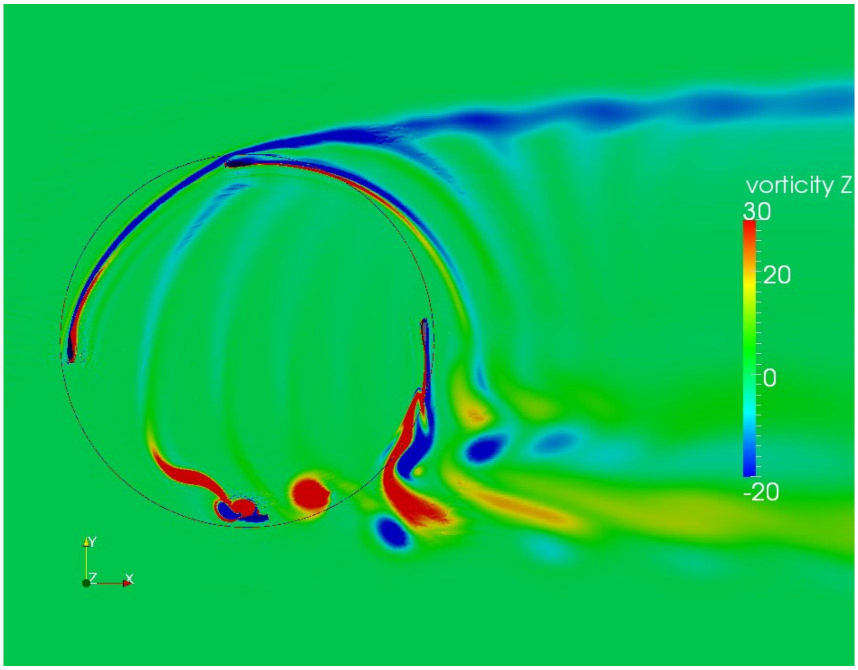

Figure 5.29. Vorticity $(1/s)$ contour at $\lambda = 2$ and $\psi = 180^{\circ}$

A clockwise vortex bubble is generated at $\psi = 150^{\circ}$ from the suction surface of the blade, Figure 5.28, and the previously detached upper surface vortex was dissipated. It should be mentioned that at $\psi = 150^{\circ}$, the positive and negative generated vortices are both seen closed to the trailing edge of the airfoil. At $\psi = 180^{\circ}$, Figure 5.29, the negative vortex bubble is separated and the detached positive vortex is interacted with the associated airfoil.

5.2.4. Vorticity Structure at $\lambda = 1$

The vorticity contours, at different blade locations, are depicted in Figures 5.30 to 5.33. It is observed that clockwise vortices in top and counter-clock-wise vortices in bottom are generated and travelled downstream by the mainstream flow and gradually dissipated.

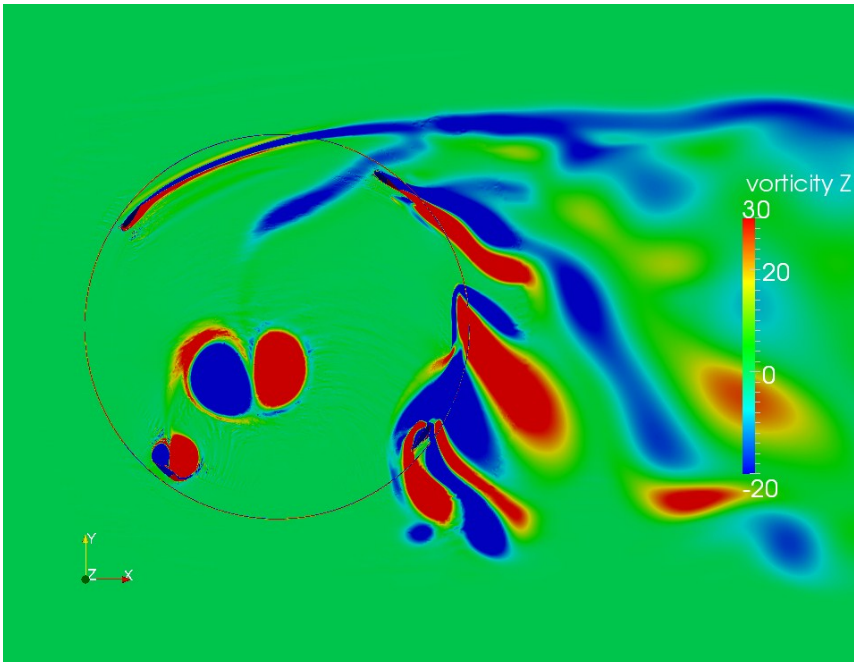

Figure 5.30. Vorticity $(1/s)$ contour at $\lambda = 1$ and $\psi = 60^{\circ}$

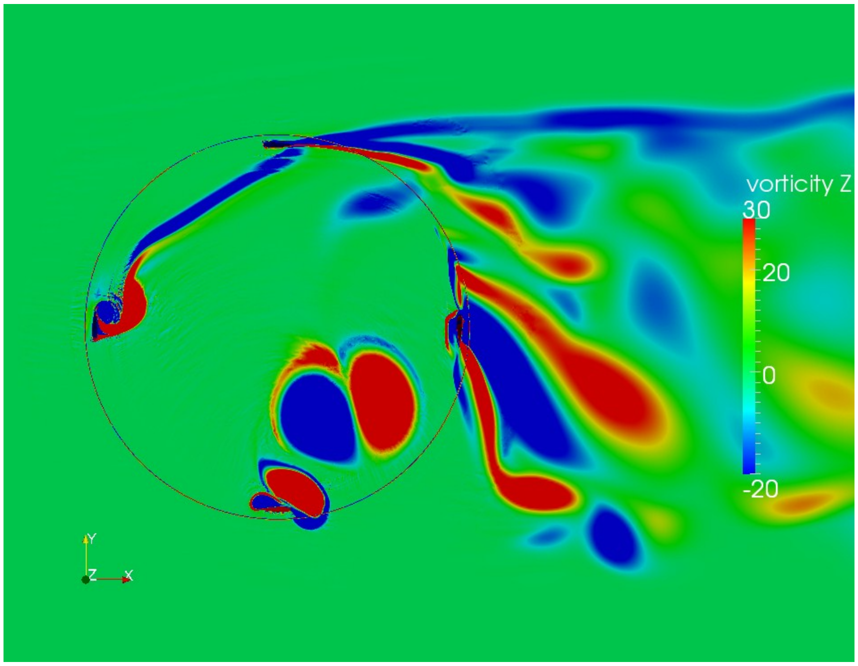

Figure 5.31. Vorticity $(1/s)$ contour at $\lambda = 1$ and $\psi = 90^{\circ}$

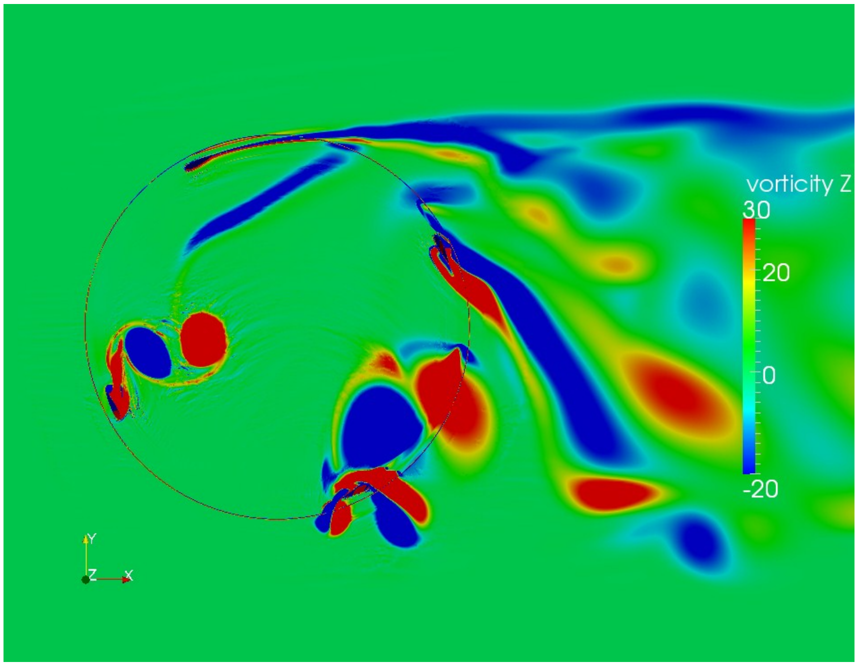

Figure 5.32. Vorticity $(1/s)$ contour at $\lambda = 1$ and $\psi = 120^{\circ}$

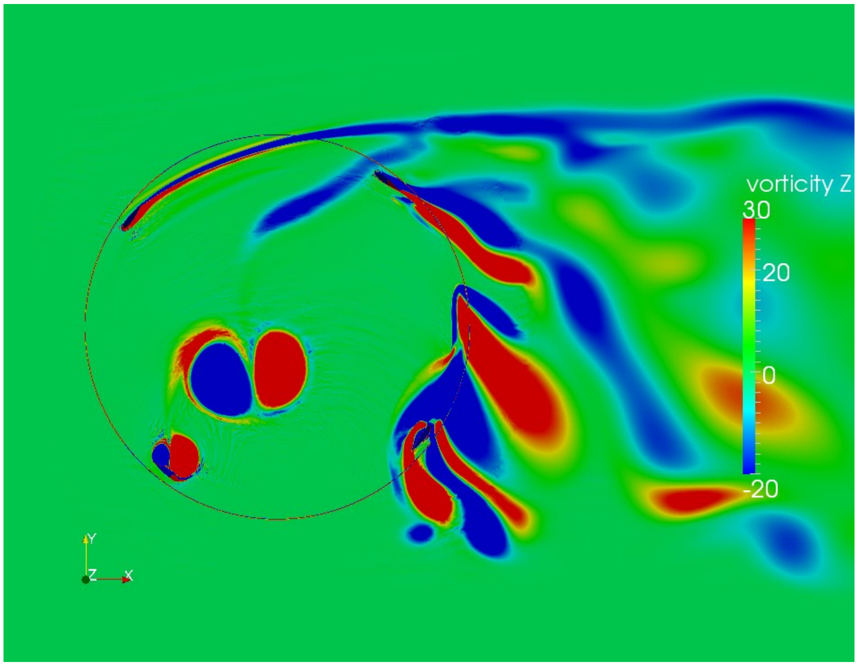

Figure 5.33. Vorticity $(1/s)$ contour at $\lambda = 1$ and $\psi = 150^{\circ}$

Figure 5.30 depicts the positive and negative vortex structures on the airfoil leading and trailing edge, respectively, At $\psi = 60^{\circ}$. Figure 5.31 shows the separation of the negative vortex from the blade at $\psi = 90^{\circ}$, where, the positive vorticity structure tends to detach the airfoil. At $\psi = 120^{\circ}$ two counter-rotating vortices, separated from the airfoil, Figure 5.32, are observed. It can also be seen that the second negative vortex starts generating from the trailing edge of the blade. Figure 5.33 shows two, rotating and counter-rotating, vortices at the middle of turbine as well as the development of negative and positive vortices at the lower surface of the blade at $\psi = 150^{\circ}$.

5.3. 2D Results of Torque vs. Azimuthal Angle

5.3.1. Torque vs. Azimuthal Angle at $\boldsymbol{\lambda = 3}$

Figure 5.34 shows the torque fluctuations at different azimuthal angles for $\lambda = 3$. There is an upward trend from 0 to 90 degrees, demonstrating the increase in the torque values. Herein, the maximum torque, after which the separation occurred, is $T = 95\ (N.m)$. After the second peak, at $T = 2\ (N.m)$, torque values declined slightly up to 360 degrees.

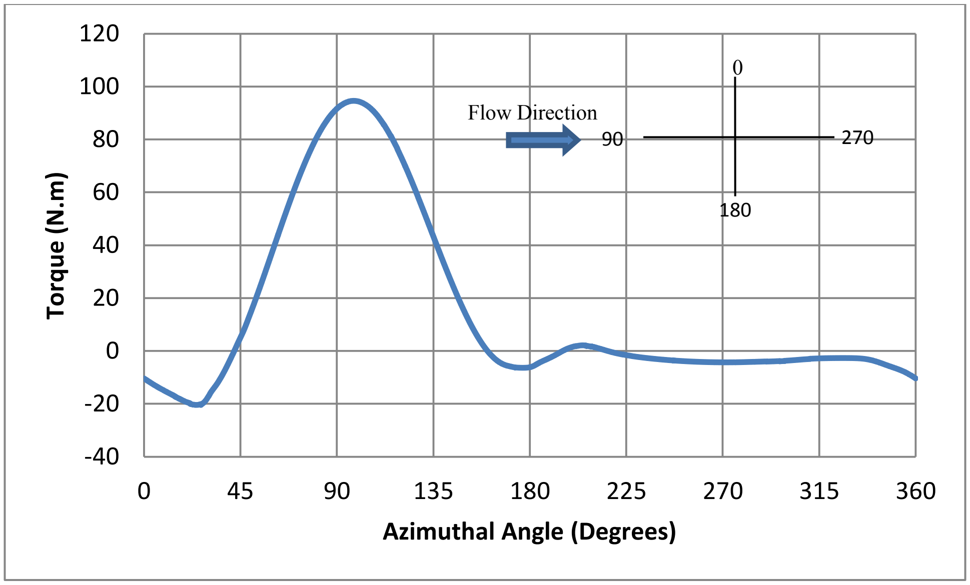

Figure 5.34. Torque variation vs. azimuthal angle at $\lambda = 3$

5.3.2. Torque vs. Azimuthal Angle at $\boldsymbol{\lambda = 2.4}$

Figure 5.35 shows the torque variation against azimuthal angle at $\lambda = 2.4$. It is observed that the azimuthal angle rose sharply from 0 to 90 degrees, where, the maximum torque, i.e., $T = 170\ (N.m)$, is achieved.

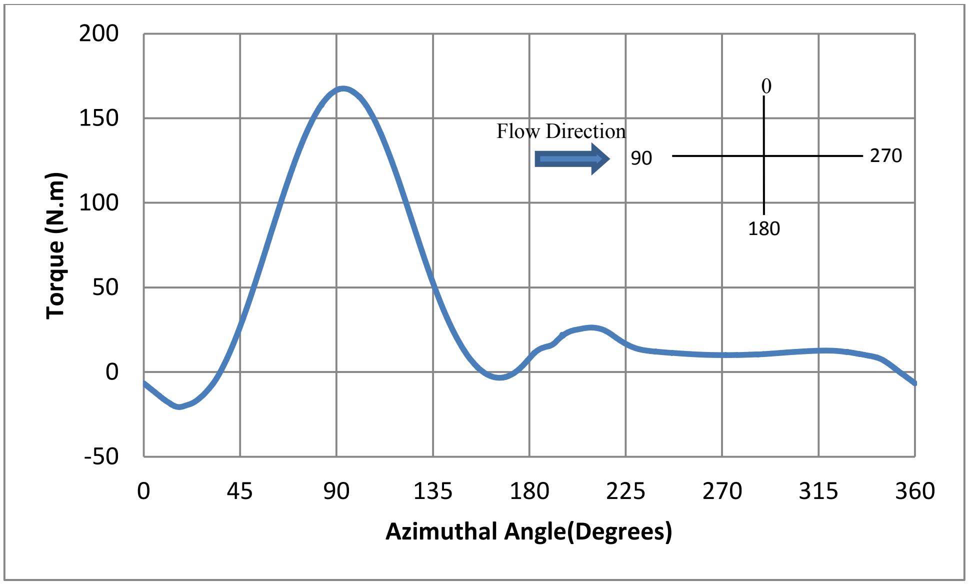

Figure 5.35. Torque vs. azimuthal angle at $\lambda = 2.4$

By passing 90 degrees, torque values are sharply fallen and then the second torque peak, i.e., $T = 25\ (N.m)$, is observed at 200 degrees. Moreover, the flow separation is occurred and the torque values are gradually decreased until it reached $T = 0\ (N.m)$ at 360 degrees.

5.3.3. Torque vs. Azimuthal Angle at $\boldsymbol{\lambda} = 2$

Figure 5.36 demonstrates the variation of torque versus azimuthal angle for $\lambda = 2$. It can be clearly seen that blade azimuthal angle is increased up to 90 degrees where it experiences its maximum torque value, i.e., $T = 250\ (N.m)$, and then a downward trend is observed where it reaches its minimum value followed by a second peak at 200 degrees. Herein, the torque is $T = 100\ (N.m)$.

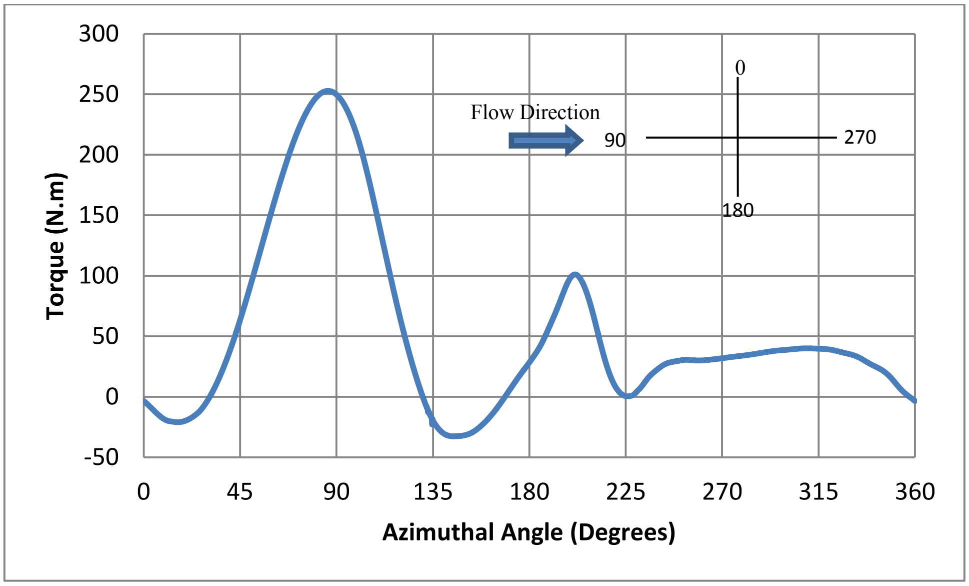

Figure 5.36. Torque variation vs. Azimuthal angle at $\lambda = 2$

5.3.4. Torque vs. Azimuthal Angle at $\lambda = 1$

Figure 5.37 illustrates the variation of torque versus azimuthal angle. By increasing the azimuthal angle from 0 degree, torque keeps increasing until it reaches its maximum, $T = 800\ (N.m)$, at 60 degrees. Herein, the maximum angle of attack of the blades occurs. Since, the angle of attack, that blade experiences, is higher among other TSRs, dynamic stall is expected to happen. By passing this point the torque is decreased and then the second peak is observed at backwind in 105 degrees. Moreover, the minimum torque, i.e., $T = -350\ (N.m)$, is observed at 85 degrees. It should be stated that other peaks which are observed in the graph are due to the interaction of the vortices with the blades.

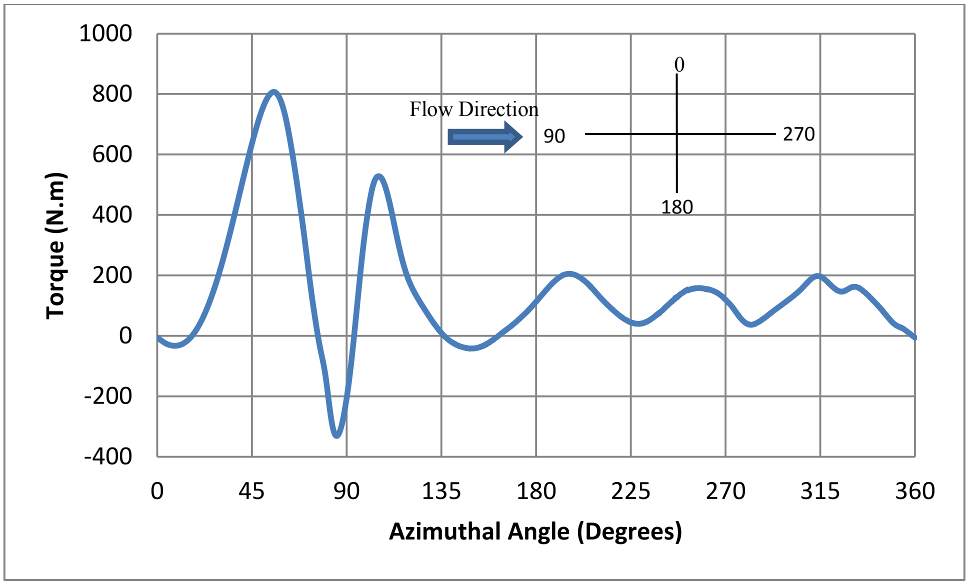

Figure 5.37. Torque variation vs. azimuthal angle at $\lambda = 1$

.

6. 3D Results and Discussion

In this chapter

The 3D flow structure is presented and the obtained 2D and 3D results are compared.

6.1. Flow Field

A 3D simulation is performed on a 16 Million 3D mesh, which is the result of the extrusion of a coarse mesh with 444 042 elements, to calculate the C_p as well as formation of tip vortex around the blades at $\lambda = 2$. It should be mentioned that the minimum time required for convergence was more than 2 months. Figure 6.1 and Figure 6.2 illustrate the tip vortex of the blades in x and y directions. It is seen that the tip vortices in centreline is helicoidal with a slightly deviation downwards, i.e. towards the inside of the rotor. This inward shift is probably due to a lower pressure inside the rotor. It can also be visualized that the tip vortex, captured in the simulation, vividly affects the flow pattern on and around the blades.

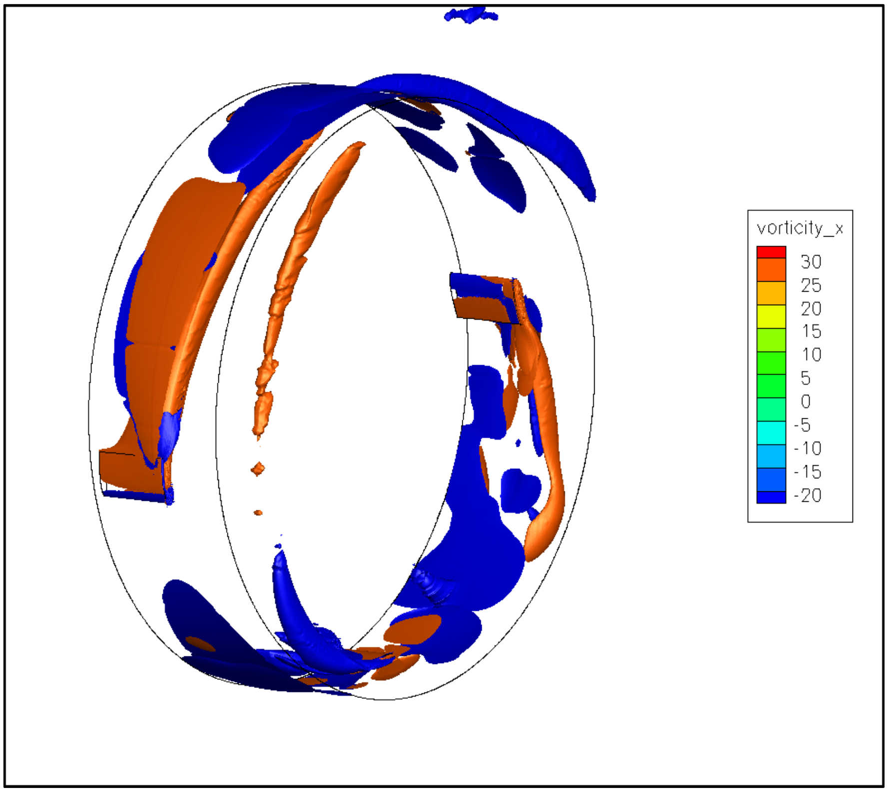

Figure 6.1. 3D vortex in x-direction $(1/s)$ at $\lambda = 2$

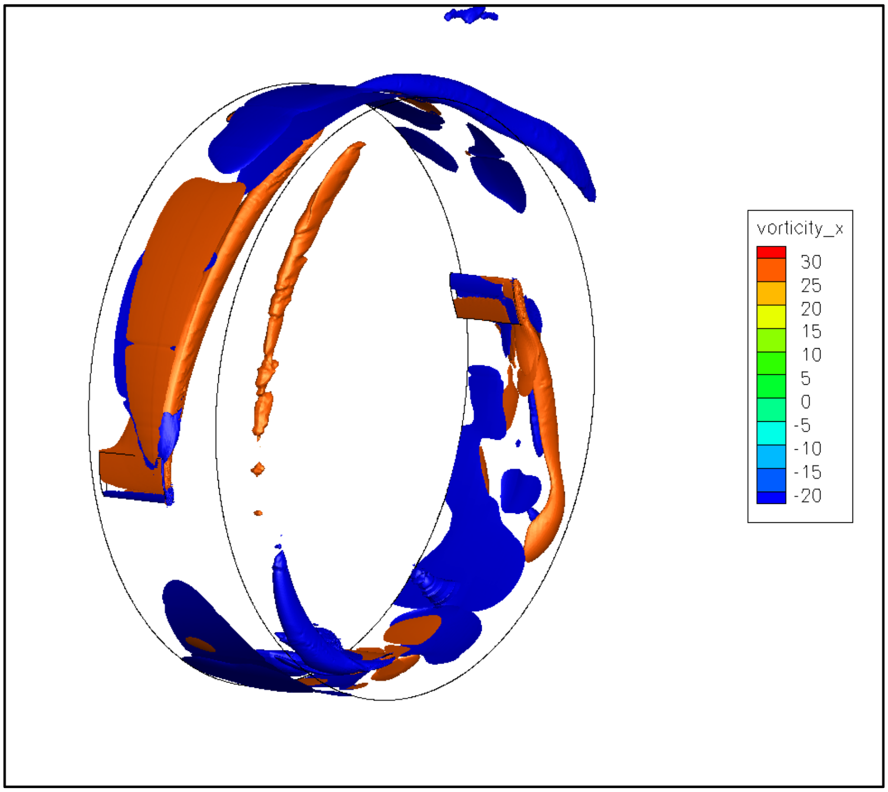

Figure 6.2. 3D vortex in y-direction $(1/s)$ at $\lambda = 2$

It can be visualized that the average value of vortices around the tip of the blades are approximately $25\,(1/s)$. Furthermore, in 3D analysis the average value of time-step ≈ 0.0003 per iteration. Figure 6.3 shows the exerted torque on each blade at $\lambda = 2$. There is an upward trend from 0 to 80 degrees, demonstrating the increase in the torque values. It can be seen that around 80 degrees, the maximum torque, i.e., $T = 130\ (N.m)$, is achieved. Afterwards, there has been a sharp decline up to 160 degrees followed by the second peak obtained at 250 degrees and the torque value of $T = 130\ (N.m)$. Also, from 250 to 360 degrees a downward trend is visualized.

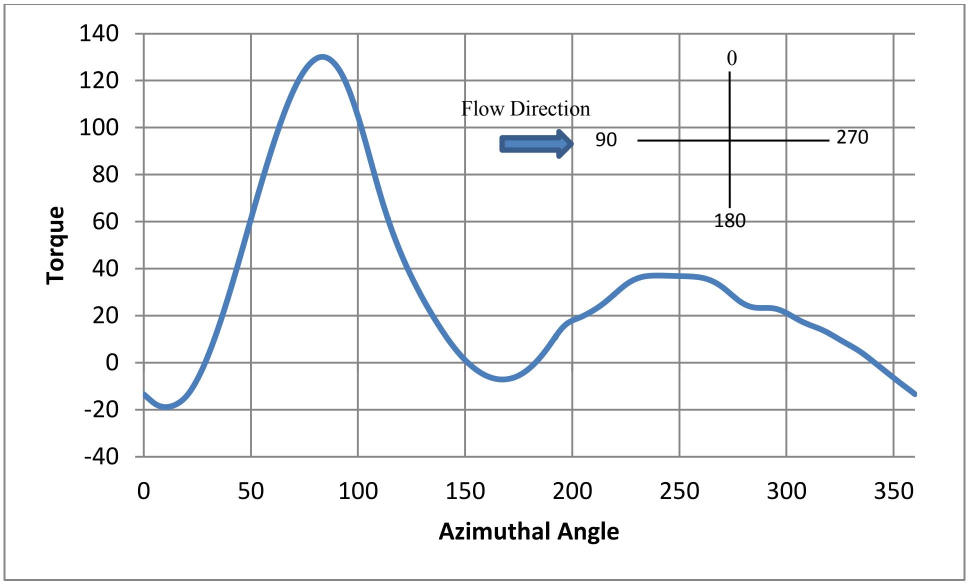

Figure 6.3. Torque vs. azimuthal angle at $\lambda = 2$ for 3D mesh

6.2. Comparison among the obtained 2D and 3D results

As it was expected, the 3D simulation results demonstrate the reduction of the turbine efficiency, compared to 2D investigations. Figure 6.4 shows that the torque curve in the second half of revolution for the very coarse 2D mesh, which is completely different from the 3D solution, Figure 6.3. The main reason lies on the mesh structure, different prediction of separation of the flow from the blades as well as the various blade-vorticity interactions between 2D and 3D simulation.

On the other hand, averaged power coefficient for 3D simulation is less than the 2D analysis for the same TSR. Therefore, by taking into account the flow structures, 3D simulation significantly under-predicts the power coefficient. The discrepancy is due to the mesh structure as well as capturing 3D eddies and vorticities on the blade including tip vortices. Furthermore, Figure 6.5 illustrates a 2D and 3D slice of z-direction vorticity at $\lambda = 2$.

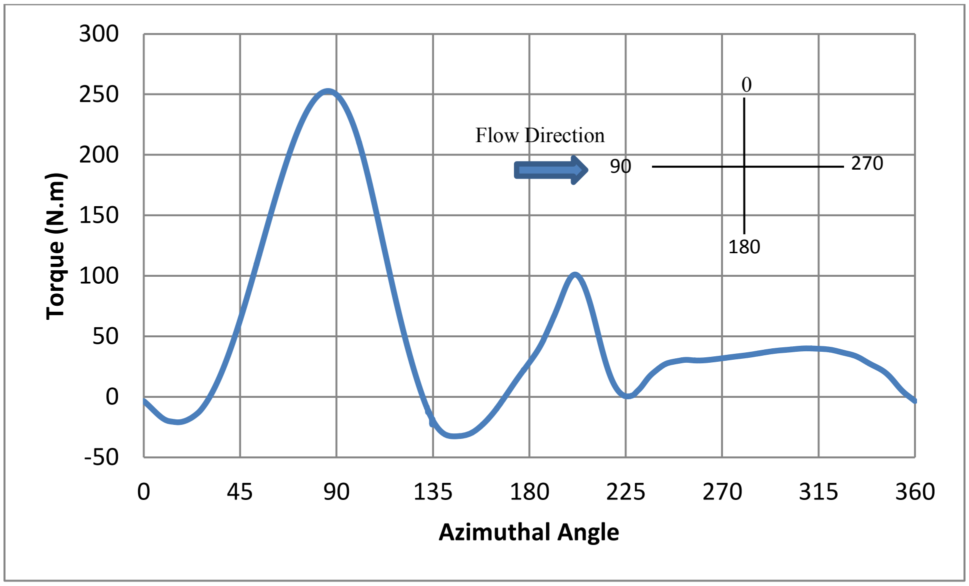

Figure 6.4. Torque vs. azimuthal angle at $\lambda = 2$ for 2D coarse mesh

It can be seen that up to 90 degrees, the same flow pattern is observed for both 2D and 3D, however, from 90 to 270 degrees, the vorticity structure is different, as less wake is captured in the 3D case. Finally, from 270 to 360 the same vorticity feature is visualized.

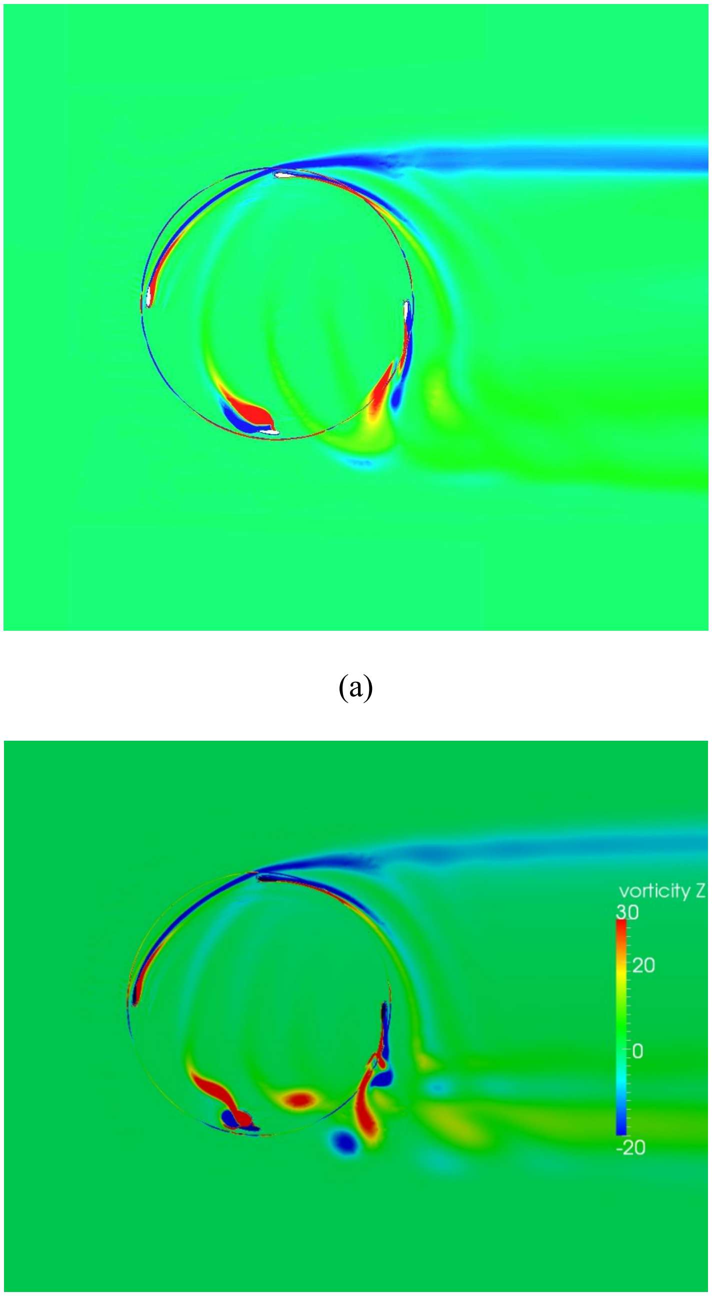

(a)

(b)

Figure 6.5. a) 3D and b) 2D slice of z-direction vorticity at $\lambda = 2$

7. Closure

In this chapter

The closure part of this numerical study, achieved goals, overall conclusion of this work and also the future works are discussed.

7.1. Conclusion and Future Works

The flow around the WHI 530G VAWT was simulated for both 2D and 3D cases. In 2D simulations, first, a grid convergence study was conducted to ensure the independency of solution to the grid resolution in the verification phase and it was identified when grid convergence requirements are met. Afterwards, the power coefficients at different tip speed ratios were calculated in order to predict the efficiency of the wind turbine at different free-stream conditions and a fixed angular velocity. It was seen that the Power Coefficient in 2D investigations, was increased with the mesh size until it achieved grid convergence. Furthermore, in the validation phase the results of the numerical analysis were quantitatively validated with the experimental values. In this CFD research the maximum efficiency was obtained at $\lambda = 2.4$ and also, the least wake generation was observed at $\lambda = 3$, compared to all the other TSRs. Finally, 3D analysis was performed at $\lambda = 2$ and it was found that only the coarse mesh could be used due to large computational requirements. Moreover, it was seen that the 3D coarse mesh significantly under-predicts the Power Coefficient but is able to capture tip vortices.

Although, in 3D investigation tip vortices have been captured, a finer mesh is required for the Coefficient of Power analysis. It should be mentioned that as an alternative solution, a powerful cluster can also be employed to accelerate the numerical investigation. Moreover, a further research and development in the advancement of the GGI algorithm is needed to support large scale simulations. In order to investigate the accuracy of the open source software package, it is necessary to conduct the simulations by using other solvers, e.g., CFX. Besides, unsteady wind analysis should be performed to investigate the coupled vortex effect for comparing the wake across the computational domain.

Finally, in order to investigate the dynamic stall in details, it is important to employ more sophisticated RANS models or LES approaches to capture the flow transition.

References

[1] Eriksson S., Bernhoff H. and Leijon M., "Evaluation of different turbine concepts for wind power," *Renewable and Sustainable Energy Reviews*, vol. 12, no. 5, pp. 1419-1434, June 2008.

[2] Paraschivoiu I., *Wind Turbine Design With Emphasis on Darieus Concept*. Montreal, Canada, 2002.

[3] Sathyajith M., *Wind Energy Fundamentals, Resource Analysis and Economics*. Netherlands: Springer-Verlag Berlin Heidelberg , 2006.

[4] Claessens M.C., "The Design and Testing of Airfoils for Application in Small Vertical Axis Wind Turbines," Delft University of Technology, M.Sc. Thesis 2006.

[5] "RENEWABLES 2010 GLOBAL STATUS REPORT," Paris, 2010.

[6] "The Global Wind Energy Outlook 2010," Brussels, 2010.

[7] (2010, August) Wikipedia. [Online]. http://en.wikipedia.org/wiki/File:HAWT_and_VAWTs_in_operation_medium.gif

[8] Wind Harvest International. [Online]. http://www.windharvest.com/

[9] Beaudoin Martin. and Jasak H., "Development of a Generalized Grid Interface for Turbomachinery simulations with OpenFOAM," , 2008.

[10] Danao M., "The Influence of Unsteady Wind on the Performance and Aerodynamics of Vertical Axis Wind Turbines," University of Sheffield , 2012.

[11] Fujisawa N. and Shibuya S., "Observations of dynamic stall on Darrieus wind turbine blades," *Journal of Wind Engineering and Industrial Aerodynamics*, vol. 89, pp. 201-214, February 2001.

[12] Simao Ferreira C., Van Bussel G. and Van Kuik G., "2d Cfd Simulation of Dynamic Stall on a Vertical Axis Wind Turbine: Verification and Validation with Piv Measurements," *45th AIAA Aerospace Sciences Meeting and Exhibit*, 2007.

[13] Simao Ferreira C., Bijl H., Van Bussel G., and Van Kuik G., "Simulating Dynamic Stall in a 2d Vawt: Modeling Strategy, Verification and Validation with Particle Image Velocimetry Data," *Journal of Physics: Conference Series*, January 2007.

[14] Wang S., Ingham D. B., Ma L., Pourkashanian M. and Tao Z., "Numerical Investigations on Dynamic Stall of Low Reynolds Number flow around oscillating airfoils," *Computers and Fluids*, vol. 39, no. 9, pp. 1529-1541, October 2010.

[15] Wang S., Ma L., Ingham D. B., Pourkashanian M. and Tao Z., "Turbulence Modelling of Deep Dynamic Stall at Low Reynolds Number," *Journal of Fluids and Structures*, vol. 33, pp. 191-209, August 2012.

[16] Simao Ferreira C., Van Zuijlen A., Bijl H., Van Bussel G. and Kan Kuik G., "Simulating dynamic stall in a two-dimensional vertical-axis wind turbine: verifi cation and validation with particle image velocimetry data," *Wind Energy*, vol. 13, no. 1, pp. 1-17, January 2010.

[17] Digraskar A., "Simulations of Flow Over Wind Turbines," University of Massachusetts Amherst, Massachusetts, M.Sc. Thesis 2010.

[18] Spalart P. R. and Allmaras S. R., "A One-Equation Turbulence Model for Aerodynamic Flows," *AIAA*, January 1992.

[19] Fares E. and Schröder W., "A General One-Equation Turbulence Model for Free Shear and Wall-Bounded Flows," *Flow, Turbulence and Combustion*, vol. 73, pp. 187-215, 2004.

[20] Tachos N.S., Filios A.E., Margaris D.P. and Kaldellis J.K., "A Computational Aerodynamics Simulation of the NREL Phase II Rotor," *The Open Mechanical*

Engineering Journal, vol. 3, pp. 9-16, 2009.

[21] Monteiro J. M. M., Pascoa1 J. C., and Brójo F. M R. P., "Simulation of the Aerodynamic Behaviour of a Micro Wind Turbine," in *International Conference on Renewable Energies and Power*, Valencia, 2009.

[22] Hamada K., Smith T. C., Durrani N., Qin N. and Howell R., "Unsteady Flow Simulation and Dynamic Stall around Vertical Axis Wind Turbine Blades," *46th AIAA Aerospaces Sciences Meeting and Exhibit*, January 2008.

[23] Edwards J., Durrani N., Howell R. and Qin N., "Wind Tunnel and Numerical Study of a Small Vertical Axis Wind Turbine," *45th AIAA Aerospace Sciences Meeting and Exhibit*, 2007.

[24] Howell R., Qin N., Edwards J. and Durrani N., "Wind tunnel and numerical study of a small vertical axis wind turbine," *Renewable Energy*, vol. 35, no. 2, pp. 412-422, February 2010.

[25] McLaren K., Tullis S. and Ziada S., "CFD Simulation of Dynamic Thrust and Radial Forces on a Vertical Axis Wind Turbine Blade," in *The 15th Annual Conference of the CFD Society of Canada*, Toronto, 2007.

[26] Edwards J. M., Danao L. A. and Howell R.J., "Novel Experimental Power Curve Determination and Computational Methods for the Performance Analysis of Vertical Axis Wind Turbines," *Journal of Solar Energy Engineering*, vol. 134, no. 3, May 2012.

[27] Duque E., Johnson W., VanDam C. P., Cortes R. and Yee K., "Numerical predictions of wind turbine power and aerodynamic loads for the NREL phase II combined experimental rotor," *AIAA/ASME Wind Energy Symposium AIAA 38th Aerospace Sciences Meeting*, January 2000.

[28] Duque E. P.N., Burklund M. D. and Johnson W., "Navier-Stokes and Comprehensive Analysis Performance Predictions of the NREL Phase VI

Experiment," *Journal of Solar Energy Engineering*, vol. 125, no. 4, pp. 457-467, November 2003.

[29] Nobile R., Vahdati M., Barlow J. and Mewburn-crook A., "Dynamic stall for a Vertical Axis Wind Turbine in a two-dimensional study," in *World Renewable Energy Congree*, Linkoping, 2011.

[30] Wikipedia. [Online]. http://en.wikipedia.org/wiki/Vertical_axis_wind_turbine

[31] (2012) Turbulence Modeling Resource. [Online]. http://turbmodels.larc.nasa.gov/spalart.html

[32] Auvinen M., Ala-Juusela J., Pedersen N. and Siikonen T., "Tme-Accurate Turbomachinery Simulations with Open-Source CFD; Flow Analysis of a Single-Channel Pump with OpenFOAM," in *V European Conference on Computational Fluid Dynamics ECCOMAS CFD 2010*, Lisbon, 2010, pp. 14-17.

[33] The open source CFD toolbox. [Online]. http://www.openfoam.com/

[34] Roache, P.J., "Verification and Validation in Computational Science and Engineering," , New Mexico, 1998.